

THESIS FOR THE DEGREE OF DOCTOR OF PHILOSOPHY IN THERMO AND
FLUID DYNAMICS

Aerothermal Experimental Investigation of LPT-OGVs

BORJA M. ROJO PEREZ

Department of Mechanics and Maritime Sciences
CHALMERS UNIVERSITY OF TECHNOLOGY

Göteborg, Sweden 2017

Aerothermal Experimental Investigation of LPT-OGVs
BORJA M. ROJO PEREZ
ISBN 978-91-7597-645-7

© BORJA M. ROJO PEREZ, 2017

Doktorsavhandlingar vid Chalmers tekniska högskola
Ny serie nr. 4326
ISSN 0346-718X
Department of Mechanics and Maritime Sciences
Chalmers University of Technology
SE-412 96 Göteborg
Sweden
Telephone: +46 (0)31-772 1000

Chalmers Reproservice
Göteborg, Sweden 2017

Aerothermal Experimental Investigation of LPT-OGVs
Thesis for the degree of Doctor of Philosophy in Thermo and Fluid Dynamics
BORJA M. ROJO PEREZ
Department of Mechanics and Maritime Sciences
Chalmers University of Technology

ABSTRACT

This thesis presents the design, commissioning, and experimental data of a newly built turbine facility at Chalmers University of Technology for investigating the flow in the engine exit structure (EES). The EES is the structure located downstream of the low-pressure turbine (LPT) in a jet engine. Flow through this structure is highly complex since non-uniformities generated at the LPT interact with the outlet guide vanes (OGVs) located inside this structure. Due to the flow complexity, a facility that can reproduce engine conditions including realistic cavities is required to validate numerical methods.

To generate realistic inlet boundary conditions for the EES, an LPT stage is located upstream of the EES. The facility is a large-scale low-speed annular cascade, and the flow Reynolds number based on the channel height of the LPT turbine stage is 465,000, which is representative for large turbofan engines. This facility follows classical low-speed wind tunnel conceptual design. Experimental correlations obtained from data collected in a previous rig and from previous studies in low-speed wind tunnels are used to compute and optimize pressure losses. CFD tools are used to evaluate the final design of the facility. A finite-element analysis of the LPT rotor and structure is performed, and a short overview of this analysis is included in the thesis.

Aero measurements were performed at several operation points of the rig for commissioning purposes. Flow periodicity and uniformity in the test section inlet are studied, and these measurements showed that the flow quality requirements are successfully fulfilled. Furthermore, experimental investigation of the EES aerodynamics and performance is performed. Data from multi-hole probe measurements and static pressure taps on two instrumented OGVs is used for this purpose. A complete set of hardware and software are developed, as well as experimental routines for high-quality aero measurements. The results from these tests show the capability of Chalmers LPT-OGV facility to reproduce LPT flow and provide high-quality data for CFD validation.

CFD calculations are performed for several operational points and compared with the obtained experimental data. Good agreement between experimental and numerical time-averaged flow quantities is achieved. The effect of the inlet boundary conditions into the EES is studied showing associated changes in the flow and performance. Analysis of the flow structures is performed based on the obtained measurement data. Finally, the results of this thesis provide a new experimental tool for evaluating novel EES designs under representative engine conditions and open-up the potential of the new facility for future research of LPT-OGV flows for the aerospace industry.

Keywords: Aerodynamics, Gas Turbine, Outlet Guide Vane, Exit Guide Vane, Engine Exit Structure, Turbine Exhaust Case, Turbine Rear Frame, Turbine Rear Structure, Wind Tunnel, Experimental, CFD, Heat transfer.

There is a driving force more powerful than steam, electricity and atomic energy: the will.
- Albert Einstein

ACKNOWLEDGEMENTS

First, I would like to thank my supervisor, Valery Chernoray, for giving me the opportunity to work on this exciting project. His support during these years was essential for me to perform the work shown in this thesis.

Thereafter, much credit goes to my co-supervisor at GKN Aerospace Sweden, Carlos Arroyo, whose advice was of incalculable value for me. His perseverance and hard work are worthy of admiration and gratitude.

Special thanks to Jonas Larsson for all his support during this time. All the inspiring discussions and help were a source of great ideas for the project. I will always be grateful for his advice.

During my work at Chalmers, Fredric Carlsvärd, Darri Kristmundsson, Carlos Jimenez Sanchez (We), and Isak Jonsson helped me with the design of the rig and to enjoy life outside my office walls. You made it easier to stand the dark, cold, and unforgiving Swedish winter. Thanks to Mirko Bovo for the great time that “We” spent in the lab and for your friendship. I would also like to thank Martin Johansson for all the discussions we had in his office and his clever advice. In addition, I would like to thank all my colleges at the fluid dynamics division who made the time in the division more enjoyable. I will always remember the unpredictability of the discussion topics during fika (coffee break).

Thanks to Monica Marcos for teaching me the value of friendship no matter the circumstances.

Last but not least important, I would like to thank my family and Sanaa for always being there to support me no matter what. Without them, I would not manage to achieve most of my goals. Gracias!

The facility was built thanks to the financial support from Energimyndigheten, Nationella flygtekniska forskningsprogrammet, the EU-commission, GKN Aerospace, and the Department of Applied Mechanics.

NOMENCLATURE

Acronyms

CFD	Computational Fluid Dynamics.
EES	Engine Exit Structure.
EGV	Exit Guide Vane.
FEA	Finite Element Analysis.
HCF	High cycle fatigue.
LCF	Low cycle fatigue.
LPT	Low-Pressure Turbine.
NACA	National Advisory Committee for Aeronautics.
NGV	Nozzle Guide Vane.
OGV	Outlet Guide Vane.
PIV	Particle image visualization.
SST	Shear Stress Transport.
TEC	Turbine Exhaust Case.
TRF	Turbine Rear Frame.
TRS	Turbine Rear Structure.

Latin

A	Amplitude of the acceleration function (m/s^2).
C_p	Static pressure coefficient.
C_{p_0}	Total pressure coefficient.
K	Pressure loss coefficient.
L	Length of the contraction duct (m).
P_T	Total pressure (Pa).
P	Static pressure (Pa).
Re	Reynolds number.
R	Radial distance (m).
S	Cross-section area (m^2).
\dot{m}	Mass flow rate (kg/s).

a	Acceleration of the fluid (m/s^2).
c	Distance from contraction inlet to beginning of damping function (m).
d	Distance from contraction inlet to end of damping function (m).
k	Turbulent kinetic energy (m^2/s^2).
p	Distance from contraction inlet to nose cone (m).
q	Dynamic pressure.
s	Parameter to define the central body.
u_0	Axial velocity at the contraction inlet (m/s).
u	Axial velocity (m/s).
x	Axial distance (m).
y^+	Dimensionless wall distance.

Greek symbols

α	Swirl angle ($^\circ$).
β	Open area ratio (%); yaw angle ($^\circ$).
δ	Absolute error.
ϵ	Turbulent dissipation rate (m^2/s^3); error of a variable.
κ	Parameter for acceleration function.
λ	Parameter for acceleration function.
ω	Specific dissipation rate ($1/s^1$); vorticity ($1/s^1$).
ρ	Air density at standard conditions (kg/m^3).

Subscripts

1	Inlet.
2	Outlet.
θ	Relative to circumferential direction.
cb	Relative to central body.
c	Relative to contraction section.
d	Relative to contraction duct.
ref	Relative to reference point.
r	Radial; relative.
x	Relative to axial direction.

Superscripts

$\bar{\cdot}$	Average.
$\tilde{\cdot}$	Mass averaged.

Contents

Abstract	i
Acknowledgements	v
Nomenclature	vii
1 Introduction	1
1.1 Description of the work	3
1.2 Aims	4
2 Experimental Facility	5
2.1 General description of the facility	5
2.2 Requirements for the facility	7
2.3 Components	7
2.3.1 Fan	7
2.3.2 Diffusing section	8
2.3.3 Flow conditioning section	12
2.3.4 Contraction section	13
2.3.5 Turbine section	19
2.3.6 Engine exit structure	28
2.4 Pressure drop calculation	29
3 Aerodynamic Measurements Setup	33
3.1 Experimental layout	33
3.2 Multi-hole probe	35
3.2.1 Uncertainty Estimation Multi-hole Probe	35
3.3 Pressure taps	40
3.3.1 Uncertainty Estimation Pressure Taps	41
3.4 Notes on Heat Transfer Experiments	42
4 Results	45
4.1 Definitions	45
4.2 Commissioning	46
4.3 Time-Averaged Flow field	50
4.3.1 Inlet plane measurements	50

4.3.2	Outlet plane measurements	53
4.4	Performance evaluation	56
4.5	CFD vs Experiments	58
5	Conclusions	63
6	Contribution to Knowledge	65
7	Summary of Papers	67
7.1	Overall Project Description	67
7.2	Paper A	68
7.3	Paper B	68
7.4	Paper C	69
7.5	Paper D	70
7.6	Paper E	70
	Bibliography	71
	Appendices	74
A	Pictures from Chalmers LPT-OGV rig	75

1 Introduction

Demands from industry to improve the efficiency of energy systems, including aero engines, are leading to research focused on more efficient propulsion systems. Energy efficiency can be increased in jet engines by increasing the by-pass ratio or introducing geared engines. As a consequence, LPT OGV¹ inlet swirl angles are increased for ungeared two-spool engines or geared engines that have increased off-design swirl variations. Therefore, LPT OGV aero design is becoming more demanding, and new experimental data on OGV designs are required.

OGVs are located downstream of the last stage of the LPT in an aero engine, as shown in fig. 1.2. The main structural purpose of this component is to connect the rear engine mounts with the low-pressure shaft bearings. The OGVs thus carry the loads from the engine. Furthermore, OGVs should provide space for oil scavenge tubes passing from the outer case to the shaft of the engine. In addition to the structural and connective functions, the OGVs also play an important aerodynamic role in an aero engine because they remove the swirl that comes from the LPT situated upstream.

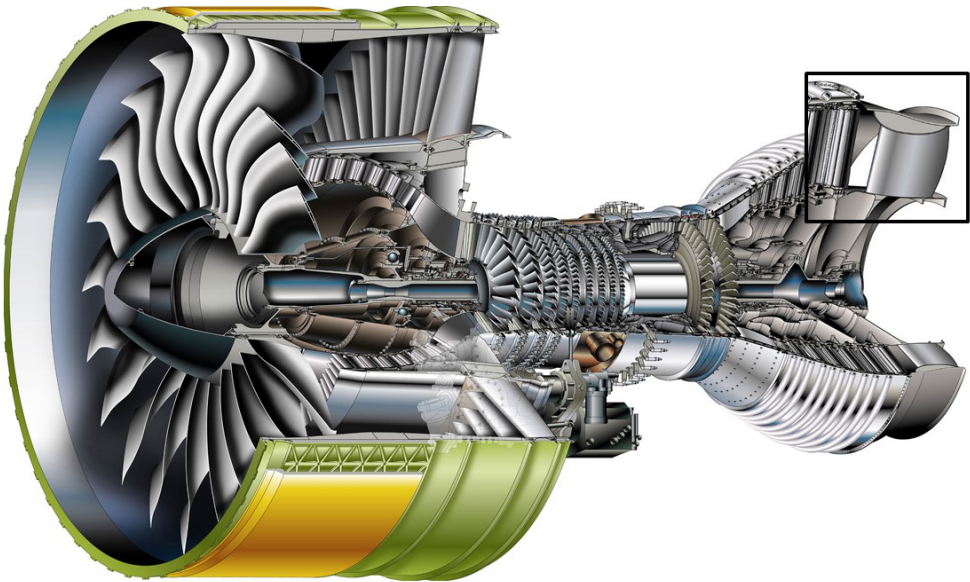


Figure 1.1: *GP7000 turbofan engine, from [1].*

The flow around an OGV is inherently complex, involving wakes from the upstream turbine (see Goldstein and Spores [2]), interaction of boundary layers, and the risk of flow separation. Due to the small number of OGVs in the EES² (typically 12), it is very important to study secondary flow. Structural requirements on the EES lead to the use of polygonal endwalls and sunken engine mounts that further complicate the aero design in

¹Also known as EGV.

²Also known as TEC, TRF or TRS.

the shroud region. The design parameters that are required from an aerodynamic point of view are the minimization of the pressure drop, flow separation margin, acceptably low enough upstream forcing to the LPT, acceptable circumferential and radial variation of swirl angle at outlet and margin to choking. Moreover, the prediction of flow separation and heat transfer becomes more crucial when the OGV has an inlet incidence angle different from the on-design operation condition. Modern geared engines show large swirl angle variations and high temperatures at off design conditions; hence, heat transfer predictions become critical and relevant validations from this type of rig are needed. Thus, it is of great interest to study large variations from on-design conditions at the inlet of the OGVs, as OGVs should be able to withstand these variations inside an aero engine.

It is worth mentioning other EES designs under research where the LPT is built in an overhung design, as shown in fig. 1.2. These new concepts would enable to create aerodynamic and aeroacoustic optimized designs of the EES without the penalty of structural requirements. In fact, numerous experimental and numerical investigations have been performed in this direction at TU Gratz regarding aerodynamically (see Selic et. al. [3]) and aeroacoustic (see Marn et. al. [4]) optimized OGV designs. However, Chalmers' LPT-OGV facility is focused on testing designs where current requirements for EES are present.

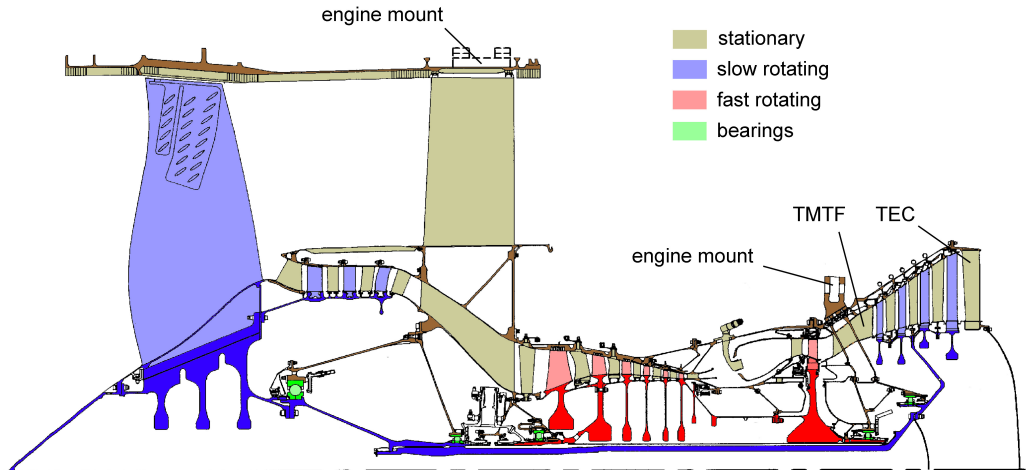


Figure 1.2: *Future engine concept, from [5]*

Although experimental data of the flow in the EES and outlet guide vanes exist, these are insufficient for CFD validation of current EES designs. Most of the experimental data available for flow around OGVs are either representative of old OGV designs or are from experiments in linear cascades (see Sonoda and Schreiber [6], Hjärne et al. [7], Hjärne [8], and Rojo et al. [9]), which are valuable for 2-D validations. Recently, Schönleitner et al. [10] showed that an annular cascade rig with an LPT upstream of the test section can provide realistic data on the complex flow inside the EES.

Hence, Chalmers' LPT-OGV rig is a unique facility for testing EES performance at realistic Reynolds number at standard atmospheric conditions. Finally, it is important

to point out that, even though current LPTs operate close to sonic conditions, most of the physical phenomena involved in the EES section are also present at low speed, such as secondary flows, rotating wakes, and interaction with the duct endwalls. Hence, the experimental data obtained from this annular cascade rig can be valuable for CFD validation and component testing. Furthermore, building a high-speed rig would have become expensive and would have been difficult to operate, and very high requirements would have been imposed on the measurement techniques.

1.1 Description of the work

This report presents the work done at Chalmers University of Technology. The designs and results presented in this thesis combine numerical and experimental work.

The main focus of this thesis is to explain the design of the LPT-OGV rig and experimental results obtained from it. As part of design this facility, methods on the aero design of most components are explained in detail and a small portion of FEA carried out for safety during facility operation and deformation prediction purposes. Regarding aero design, GKN Aerospace Sweden provided the aero surfaces of the LPT stator-rotor stage and EES that will be tested in this facility. The rest of the components were designed at Chalmers University of Technology.

At the beginning of the project, an upgrade of an existing facility (see Arroyo [11]) was thought to be sufficient to provide a realistic Reynolds number in the test section. Then, after several design iterations, the construction of a larger facility was found necessary to achieve realistic engine Reynolds numbers in the test section. Hence, all components of this new facility needed to be designed from scratch. For the design of the facility, CFD tools were used to analyze most of the components inside the facility. The goals of these studies were to obtain the required flow quality in each section and to optimize the length of some components. A thermal design of the facility and hydraulic system to connect the different components was also done. This work took over two and a half years.

Once components started arriving at Chalmers, the assembly process took one and a half years. During this time, flow quality measurements at the outlet of flow conditioning and the outlet of the annular screen were performed. Also, some work was put in on the redesign of the structural components since resonance frequencies were found inside the operating range. In addition, electronic instrumentation of this facility was carried out at Chalmers. Moreover, time was spent on setting up this facility to be remotely controlled. Afterwards, when the turbine and test section were assembled, 360° mid-span measurements were performed to study flow periodicity at the outlet of the test section. Since February 2017, the Chalmers LPT-OGV facility has been operating continuously and data from multi-hole probe measurements and static pressure taps are shown in this thesis.

Finally, CFD validation work was performed. The numerical mesh was produced at GKN Aerospace Sweden and numerical simulations were performed at Chalmers University of Technology using ANSYS CFX commercial software.

1.2 Aims

This research aims to investigate the highly complex flows from an LPT to an EES and their influence on aero performance and heat transfer. This will lead to a better understanding of the phenomena involved in this section of the engine and provide validation data for CFD.

The pressure losses inside the EES is of great interest for validation of the tools used for the design of the EES. In addition, it is very important to study secondary flows because a low aspect ratio in the EES designs is more sensitive to changes in the inlet flow. Predicting flow separation is of great interest as well because of the complexity of the flow inside this section. Studying these phenomena at on-design and off-design conditions will lead to the development of more robust aero designs. Predicting transition phenomena is complex, and they have a substantial influence on the flow structures and heat transfer over the OGVs.

In sum, the main purpose of this work is to design, build, and test a large-scale, low-speed LPT-OGV facility to investigate aero performance of state-of-the-art EESs and enable the use of future (and more sophisticated) measurement techniques to obtain valuable data for the turbomachinery scientific community. Furthermore, non-conformances from manufacturing methods and surface roughness are examples of study cases that could be relevant for the turbomachinery industry.

2 Experimental Facility

2.1 General description of the facility

The rig is set to be a closed loop facility where an LPT is located upstream of the test section to provide engine-realistic inlet boundary conditions to the EES. There is a return channel downstream of the EES that connects the flow outlet from the test section to a centrifugal fan. Figure 2.1 shows the rig layout. There is a centrifugal blower that is driven by an electrical motor. A straight duct is located downstream of the fan outlet to obtain better flow with minimal losses in the rest of the facility and less noise generation (especially in the diffusing section). Afterwards, there is a vaned corner duct and a diffuser duct (see 2.3.2 and 2.3.2). The diffusing angle was selected to be as low as possible to reduce the risk of large flow separation and unsteadiness. There is a second diffuser duct after the second vaned corner to obtain a 2x2-meters square cross section.

The flow is cooled after the diffusers to approximately 20°C in a heat exchanger. It is important to control the flow temperature since one of the requirements for this facility is a steady flow with good repeatability. Heat transfer experiments will be performed in the future, and this makes having a controlled steady temperature crucial. Furthermore, the heat exchanger produces the second highest pressure loss in the rig, and this will be helpful in increasing flow uniformity and reducing the losses in the settling chamber located downstream of this section. Most low-speed wind tunnels situate the heat exchanger upstream of the flow conditioning section (see Bradshaw and Pankhurst [12]).

A honeycomb and five screens are in the settling chamber to improve the flow uniformity. The honeycomb is used to remove swirl flow and cross velocity fluctuations. Turbulence screens are used to make the flow uniform. The contraction duct with the central body is downstream of this section. After this contraction, an annular straight section drives the flow from the contraction section to the LPT stage. There are two rows of four NACA 0020 struts and a turbulence screen in between to remove the wakes generated by these struts. The LPT stage has 60 NGVs at the stator and 72 blades at the rotor. The rotor blades are shrouded, and the tip flow leakage is representative of aero engines in terms of mass and the flow ratio between the main flow and the leakage flow. To control the rotational speed of the turbine, a hydraulic pump is connected to the rotor's shaft. Afterwards, the flow passes through the EES, where most of the measurements will take place. Purge flow coming from the rotor cavity and passing through the rim seal will be included and will interact with the main flow. Although the EES is the main component that will be studied, it has an additional function in this facility, which is to straighten the flow coming from the LPT. The outlet flow coming from EES should, therefore, be fully axial. Finally, the flow at the outlet of this section will return to the fan inlet.

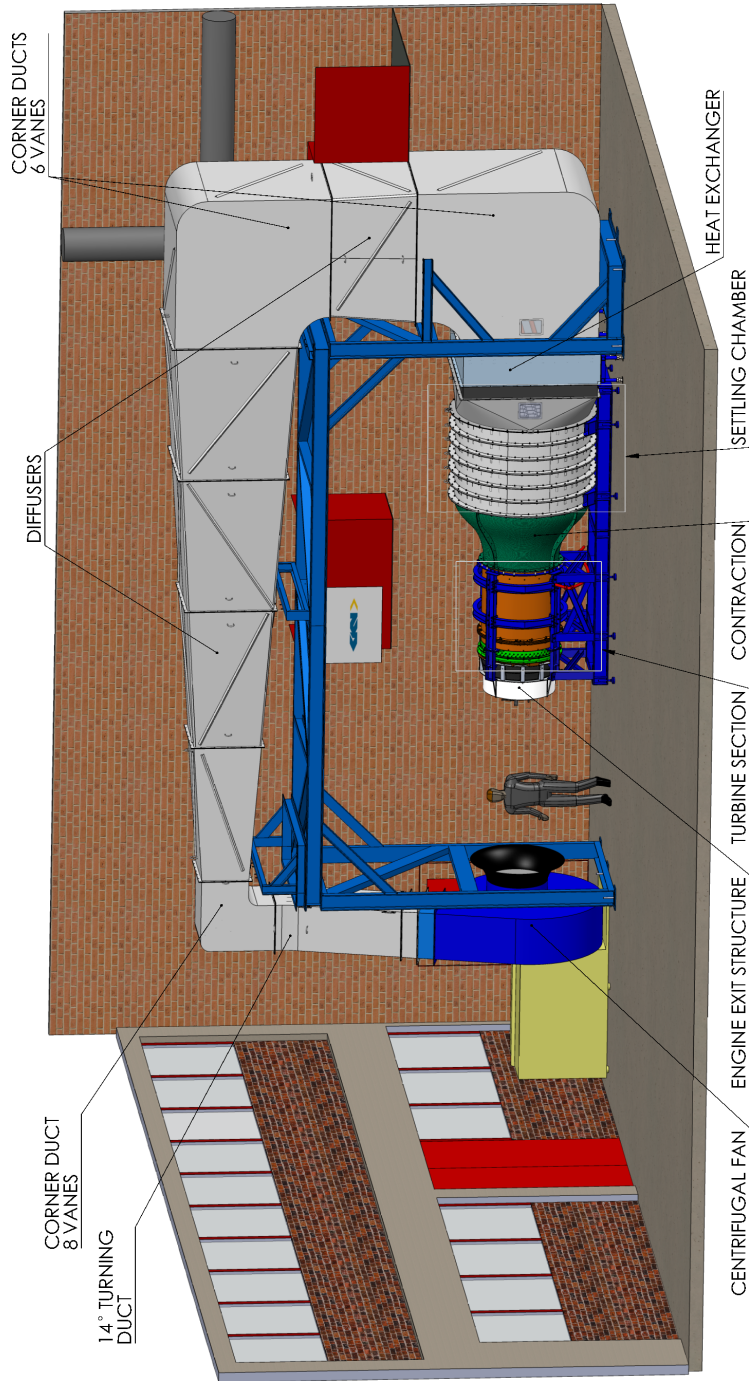


Figure 2.1: *Rig layout.*

2.2 Requirements for the facility

The main requirements of this facility are listed below.

- **Reynolds number similarity.** It is important to have a Reynolds number at the inlet of the turbine stage and EES section that is similar to what can be found in a real aero engine in order to achieve flow characteristics comparable with a real engine. In this facility, the Reynolds number is about 450,000 based on the axial chord of the OGVs. For large ungeared engines, the Reynolds number can be around 450,000 and, for a smaller engine such as a geared turbofan engine, the Reynolds number can be over 300,000.
- **Stable operating conditions and repeatability.** In this experimental rig, a steady flow (velocity, pressure, and temperature) is needed into the turbine stage and EES. Furthermore, the same results should be obtained under the same conditions in this facility.
- **Representative inlet flow to the EES.** It is required that the flow from the turbine has representative wakes and secondary flows, swirl, and mass flow distributions, tip leakage flow, and rim-seal purge flow. It should be possible to cover important off-design variations (from -6.4° to -26.4°) and to vary Re numbers.
- **Access for the measurement techniques.** Access and traversing systems for the different measurement techniques should be provided, while the disturbances to the flow should be kept to a minimum.
- **Modular design.** A modular design will enable exchanging the EES and testing different configurations.
- **CFD friendly.** To decrease the computational resources needed for CFD simulations, the ratio between the number of NGVs and/or rotor blades and OGVs should be a low integer number (in our case 60/72/12).

2.3 Components

This section explains the function and design criteria of all the components used in this experimental facility.

2.3.1 Fan

The centrifugal fan was selected to provide the required flow rate and pressure. Classical low-speed wind tunnels use an axial fan because it can provide a higher mass flow than a centrifugal blower but a lower pressure ratio. Due to the high pressure drop required to run the turbine, a centrifugal blower was selected. A frequency converter drives the motor and allows for a continuous regulation of the mass flow rate in the facility. Elastic connections are used between the fan and the rest of the facility to avoid propagating

Table 2.1: Fan main characteristics.

Parameter	Value
Design volume flow rate (m^3/h)	6900
Design total pressure (kPa)	7.56
Fan wheel diameter (mm)	1620
Maximum rotational speed (rpm)	1800
Electric motor maximum power (kW)	200
Total efficiency	0.82
Noise levels (dB)	114.1

the vibrations of the fan to the neighboring components. Table 2.1 shows the main characteristics of the fan unit.

A straight duct is located downstream of the elastic connector. The purpose of having this duct is to obtain a more uniform flow into the diffusing section and, therefore, lower aero losses and noise.

2.3.2 Diffusing section

Because the pressure losses in the heat exchanger and flow conditioning are proportional to the velocity square and function of the Reynolds number, the air flow coming from the centrifugal fan outlet (a rectangular section of 710x900 mm) must be diffused to a larger cross section area (a square section of 2,000x2,000 mm) to reduce the pressure required to drive the given flow through the facility. The most important requirements for this section are to provide the area change and turn the flow with minimum losses, flow separation, and non-uniformities.

Corner design

All the corners have been designed according to the guidelines found in Barlow et al. [13]. These corners are equipped with guide vanes, which are bent plates with a straight trailing edge. Thick, solid vanes generate more uniform flow, but constant thickness vanes made of thin plates are more economical and can deliver the required performance.

Due to the high Reynolds number at the inlet of these components (over 500,000), the gap-chord ratio chosen for the guide vane design is 1:4 (see Barlow et al. [13]). The first corner contains eight vanes and the second contains six vanes. The third corner is a scaled-up design of the second corner.

CFD analysis verified the aero design of this component and showed good agreement with empirical data.

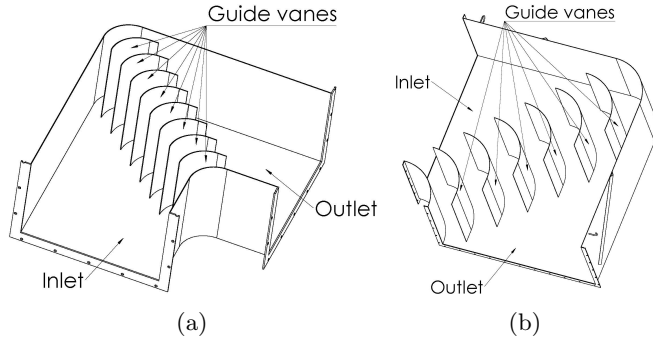


Figure 2.2: a) Section view of the first vaned corner b) Section view of the second and third vaned corner.

Diffusers design

In classical low-speed wind tunnel design, the diffuser is one of the most important components. A bad diffuser design can lead to high losses, noise generation, and non-uniform flow even if there is a settling chamber. Therefore, this component was designed with the smallest diffuser angle possible (there is space limitation in the facility). Both diffuser ducts have the same diffuser half angle of 3.75° .

The fact that the flow velocity profile at the outlet of the centrifugal fan is unknown and not uniform might increase the losses in the diffusing section and cause flow non-uniformity. For this reason, the possibility of adding a turbulence screen inside the first square diffuser was provided. This is explained in detail in section 2.3.2.

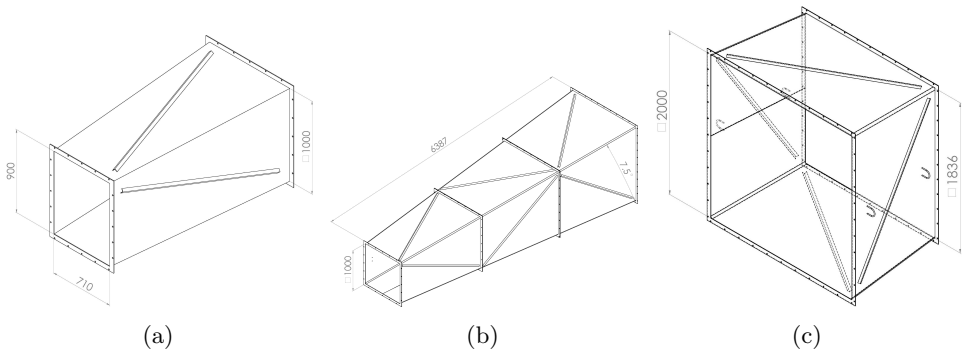


Figure 2.3: a) Rectangular to square section diffuser duct b) First square diffuser duct c) Second square diffuser duct between second and third corners.

CFD analysis of the diffusing section

Using CFD analysis, different configurations were evaluated for the design of the diffusing section. First, a 2-D steady state study was performed to obtain an approximate value

for the pressure losses and velocity distribution. In this study, a uniform velocity was set as the inlet boundary condition and outflow at the outlet of the diffusing section. A constant pressure drop coefficient was set in the heat exchanger, which is calculated from data given by the manufacturer of this component. The numerical grids were generated in ICEM ANSYS, and FLUENT was used as a solver. Figure 2.4 shows the effect of locating guide vanes inside the corners. The pressure losses are reduced 11%, and there are no recirculation areas where aeroacoustic noise is generated.

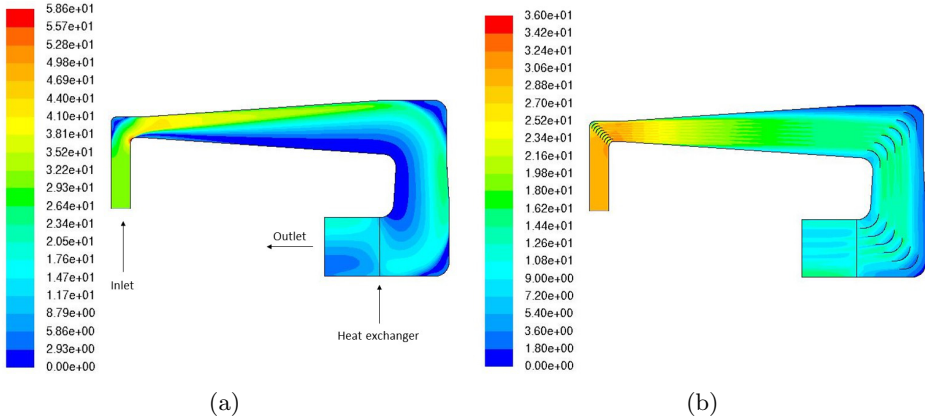


Figure 2.4: Velocity field from 2-D CFD simulation without guide vanes in the corner ducts, b) Velocity field adding guide vanes. Both simulations are performed using the $k-\omega$ SST turbulence model with $y^+ < 1$.

Furthermore, $k-\omega$ SST and $k-\epsilon$ turbulence models were compared, obtaining similar pressure losses (less than 0.1% difference). The $k-\epsilon$ model shows a slightly more uniform velocity distribution at the outlet, but not significant enough to consider further studies on the selection of a turbulence model.

The vaned 2-D case was analyzed with two different meshes. The main purpose was to check the dependency of the result on the use of wall functions ($40 < y^+ < 100$) or having resolved boundary layers ($y^+ < 1$). Both cases were studied using the $k-\omega$ SST model. This study showed that the difference between these two cases in terms of pressure losses is a 0.25% higher pressure loss using wall functions. Regarding the velocity distribution, there are no differences between these cases. Hence, wall functions can be used in the 3-D case since it is computationally less expensive. Figure 2.5 shows the numerical mesh for the 3-D case. The mesh contains 6.7M cells, and it is structured.

The main goals of this CFD simulation are to obtain the pressure losses with a realistic geometry, the influence of having a 14° turning downstream of the fan outlet on the diffuser performance, and the effect of a corner vortex on the pressure losses which the 2-D CFD cannot predict. Also, the effects of locating a turbulence grid inside the long diffuser duct are studied as is a suitable location for it in case it is needed. For this study, the $k-\omega$ SST turbulence model was used. Uniform velocity inlet boundary conditions were used and outflow at the outlet.

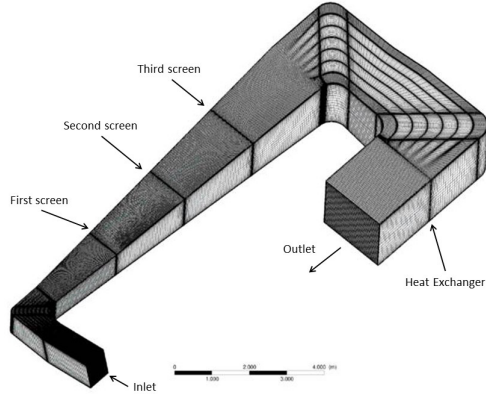


Figure 2.5: *Computational mesh for the full diffusing section.*

Figure 2.6 shows a comparison between the case without grids and the position selected for the location of a turbulence grid. To select the suitable location for the screen, three locations (first, second, and third) and different pressure drops for each screen were checked.

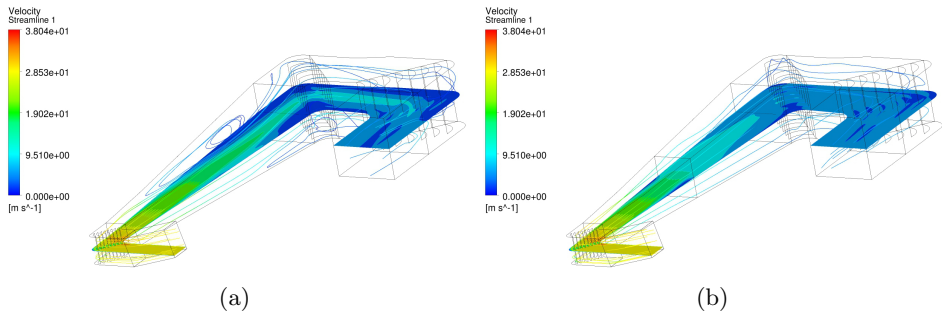


Figure 2.6: *a) Velocity distribution inside the diffusing section without turbulence grids. b) Velocity distribution with a turbulence grid located in the middle of the long diffuser duct.*

First, a large separation in the top-left corner of the long diffuser duct can be observed in fig. 2.6 a). This flow structure is much larger than in the other three corners of the diffuser duct for two different reasons. First, looking at fig. 2.4, the velocity is not symmetric with respect to the centerline of the first diffuser duct due to overturning the flow in the first corner. Having a slightly larger angle between the leading and the trailing edges of the vanes would fix this. Also, the area where the velocity starts to become non-symmetric in fig. 2.4 b) is the same as for the corner separation. Second, the lack of guide vanes inside the 14° turning duct leads to a non-uniform velocity distribution at the outlet of the first corner duct and, therefore, a larger separation on the top-left corner and a larger corner vortex on the top-right corner of the diffuser.

On the other hand, a turbulence grid could remove the large corner recirculation,

giving a more uniform profile at the outlet of the heat exchanger. Also, guide vanes have been added to the 14° turning duct to avoid having such a large corner separation. It is important to point out that these CFD simulations are performed under the assumption of a uniform flow inlet, which is not the case. No data are available from the manufacturer regarding flow or pressure distribution at the outlet of the fan. In any case, even if there are large flow structures or a non-uniform velocity distribution from the centrifugal fan, having a heat exchanger and adding a turbulence screen will lead to a satisfactory flow quality coming into the flow conditioning section.

2.3.3 Flow conditioning section

The flow from the heat exchanger has a non-uniform distribution. There are several sources of non-uniformities in the existing facility. First, the centrifugal fan generates wakes and secondary flows that might not be dissipated through the diffusing section. Moreover, the guide vanes located in the corners and the 14° turning duct also generate wakes, which can be seen in figs. 2.4 and 2.6. Furthermore, due to geometric tolerances and the manufacturing process, there is no guarantee that all the guide vanes are in the correct position, and flow non-uniformities are created in the diffusing section. Also, the flow can be affected by the negative pressure gradient inside the diffuser ducts, generating areas with high velocities and low velocities or, in some cases, flow separation. The approach taken to solve this problem is to use a honeycomb to reduce the transversal velocity components and a set of turbulence screens to obtain higher flow uniformity. Figure 2.7 illustrates the arrangement of these components.

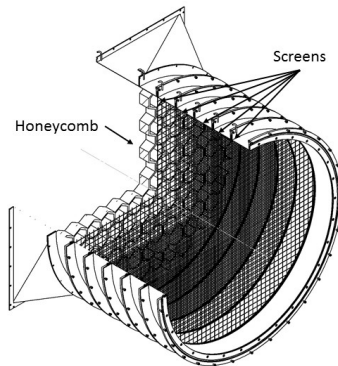


Figure 2.7: *Computational mesh for the full diffusing section*

The flow should go through a contraction duct to change the square cross section (2x2 meters) coming from the heat exchanger to a circular section with a diameter of two meters. To minimize the length of the square to circular section duct, CFD was performed to check whether corner separation generated in this duct could be removed. The length chosen for this duct after numerical analysis is 500 mm.

The air flow then passes through a honeycomb. The honeycomb is used in low-speed wind tunnels as a guiding device through which air filaments are rendered parallel

(definition given by Prandtl). A non-uniform axial velocity distribution can be expected downstream of the honeycomb. The honeycomb chosen has hexagonal cells with a length of 110 mm, a hydraulic diameter of 14 mm, and a length-to-cell diameter of 8. These values are as recommended in Barlow et al. [13] and Mehta and Bradshaw [14].

Finally, the air flow passes through five turbulence screens to reduce flow non-uniformities in the axial direction and turbulence intensity. According to Barlow et al. [9], the best result can be obtained with several screens with a coarser to finer mesh size and wire diameter, each a turbulence screen with an equivalent pressure drop coefficient. Groth and Johansson [11] suggest starting with a relatively coarse grid followed by a finer one.

Table 2.2: Main screen parameters. Pressure loss coefficient (K) calculated according to Barlow et al. [13].

Screen number	1	2	3	4	5
Cell width [mm]	4	2.5	1.75	1.25	1
Wire diam. [mm]	1	0.7	0.5	0.33	0.24
β [%]	64	61	60	63	65
Wire Re	387	271	194	128	93
K	0.75	1.01	1.13	1.1	1.01

2.3.4 Contraction section

The contraction connects the outlet of the flow conditioning section with the straight annular section of the turbine. This is done by placing a central body in front of the hub pipe and a contraction duct with a length of 1 meter. Another use of this contraction is to measure the mass flow inside the facility using the pressure at the inlet and outlet. This application of the contraction is widely used in wind tunnels and is similar to a Venturi meter. The main requirements that the contraction must fulfill are listed below.

- **Minimum contraction length:** It is critical to design a short contraction so that there is enough space to place the turbine section and EES in the facility. Therefore, the first parameter that is considered is the length of the contraction. In this case, a 1 m length contraction was achieved with an area ratio of 4.7 and a length to inlet diameter ratio of 0.5.
- **Flow quality:** Generally, contractions are not sources of high pressure drops, and, furthermore, the flow quality (from a wind tunnel perspective) can be increased if the contraction is correctly designed. Hence, once the contraction has been designed, CFD techniques are used to check that the flow quality at the outlet is good enough for our purposes.

Aero design

In an extensive literature search of this kind of contraction, no reports or examples of contraction design with a central body criterion were found (see Morel [15], Mikhail [16], Abbaspour and Shojae[17], Bell and Mehta [18], Chmielewski [19]). For the geometry calculation, the air flow is assumed incompressible, inviscid, irrotational, and axisymmetric. Furthermore, only the mean axial speed and acceleration of the fluid are analyzed (1-D problem).

$$a(x) = u \frac{\partial u}{\partial x} \quad (2.1)$$

Using all the assumptions listed above, the expression for the flow acceleration becomes as shown in eq. 2.1. This could lead to an analytic solution in simple cases, That is, axisymmetric contraction design without a central body based on a continuous acceleration function (see Chmielewski, [19]). Unfortunately, the central body produces a discontinuity in the acceleration function.

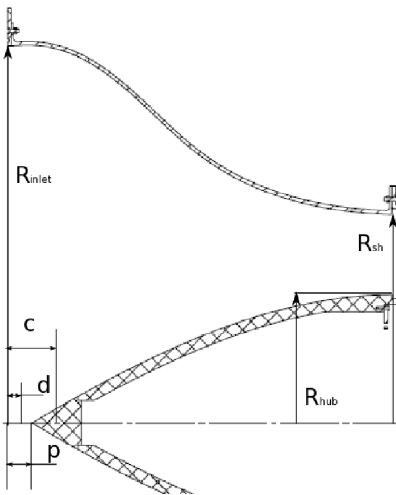


Figure 2.8: *Cross-section of the contraction.*

Furthermore, the acceleration function that provides the best shape for the duct and central body is not known. The following acceleration function has been used which is similar to the function used by Chmielewski [19] for a contraction without a central body.

$$a(x) = A \cdot f(x) = A \cdot \left[\sin \left(\frac{\pi x}{L} \right)^\kappa \right]^\lambda \quad (2.2)$$

Here $x \in [0, L]$ and $f(x) \geq 0$ for all x inside this interval. κ and λ are parameters and A is a constant. Now, the next step is to calculate the value of the constant A (or

amplitude of the function). To calculate this value, it is necessary to integrate eq. 2.1.

$$a(x) = u \frac{\partial u}{\partial x} \Rightarrow \int_0^x a(x) dx = \int_0^x u du \Rightarrow \frac{u(x)^2 - u_0^2}{2} = A \int_0^x f(x) dx$$

$$u(x) = \sqrt{2A \int_0^x f(x) dx + u_0^2} \quad (2.3)$$

Equation 2.3 is also used later for the calculation of the velocity distribution through the contraction. The velocity at the outlet is found using the mass conservation equation. A is calculated with eq. 2.4.

$$A = \frac{u(L)^2 - u_0^2}{2 \int_0^L f(x) dx} \quad (2.4)$$

Looking at eqs. 2.3 and 2.4, the only restriction on the definition of the function is that it must be integrable, which means that this method can be used even if $f(x)$ is not continuous. In the case of a central body, the acceleration function will be integrable but not continuous. To define the acceleration function, a set of three parameters is added: d , p and c (see fig. 2.8). First, a constant acceleration below the ideal curve is kept so that it damps the effect of the central body on the calculation of the contraction duct. Hence, from d , the acceleration is kept constant. Parameter p shows where the nose cone should be located. Finally, c represents where the value of the acceleration without a central body and the value of the acceleration with a central body are the same. The acceleration function can thus be defined as follows:

$$f(x) = \begin{cases} \left[\sin \left(\frac{\pi x}{L} \right)^\kappa \right]^\lambda & \text{if } 0 \leq x \leq d \cup x \geq c \\ f(d) & \text{if } d < x \leq p \\ f(c) & \text{if } p < x < c \end{cases} \quad (2.5)$$

It is important to point out that, with this method, only the duct shape is calculated based on the acceleration curve. The central body is designed using a 3^{rd} -order polynomial. The boundary conditions for the polynomial are listed below.

$$B.C \text{ for } R_{cb}(x) = \begin{cases} R_{cb}(x=p) = 0 \\ \left. \frac{\partial R_{cb}(x)}{\partial x} \right|_{x=p} = s \\ R_{cb}(x=L) = R_{hub} \\ \left. \frac{\partial R_{cb}(x)}{\partial x} \right|_{x=L} = 0 \end{cases} \quad (2.6)$$

In our case, we select $s = 0.6$ and $p = 0.05$ to obtain a smooth shape that does not have an inflection point. Finally, the geometry of the duct is calculated using the mass conservation equation for incompressible flow.

$$S = \frac{\dot{m}}{\rho u} \quad (2.7)$$

$$R_d(x) = \begin{cases} \sqrt{\frac{\dot{m}}{\pi \rho u}} & \text{if } x \leq p \\ \sqrt{\frac{\dot{m}}{\pi \rho u} + R_{cb}(x)} & \text{if } x > p \end{cases} \quad (2.8)$$

A 2-D axisymmetric CFD simulation was made to validate the performance of the designed contraction shape. The CFD results are shown in fig. 2.9. It was concluded that the contraction fulfills all our demands in terms of flow quality (no flow separation and less than 1% flow non-uniformity at the contraction outlet) and length (1 meter long). Figure 2.10 shows an example of a contraction design with lower flow uniformity due to the aggressive shape of the contraction duct and the zero curvature at the end of the central body.

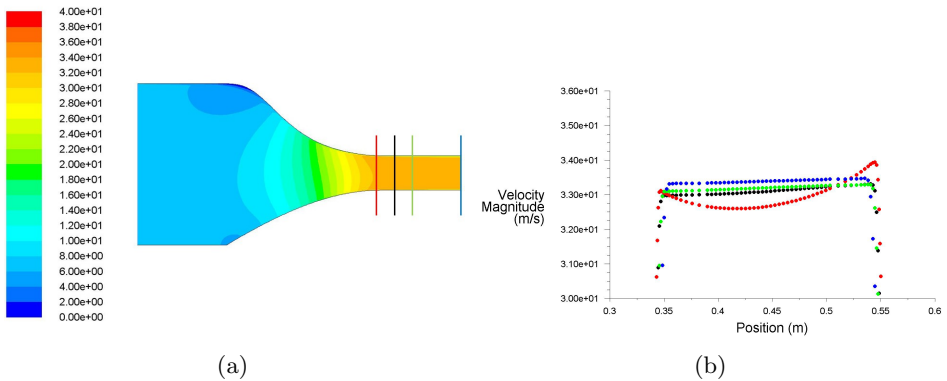


Figure 2.9: *a) Velocity contour plot of contraction's half section. b) Velocity profile at the exit of the contraction at different positions.*

Furthermore, the duct has been manufactured in four sectors bolted to each other with 5mm laminated glass fiber. FEA was performed and a maximum deformation lower than 0.1mm was obtained, which is negligible compared with the size of the duct. The central body has been manufactured with a glass fiber shell and a stereo foam core. Figure 2.11 shows images of these components.

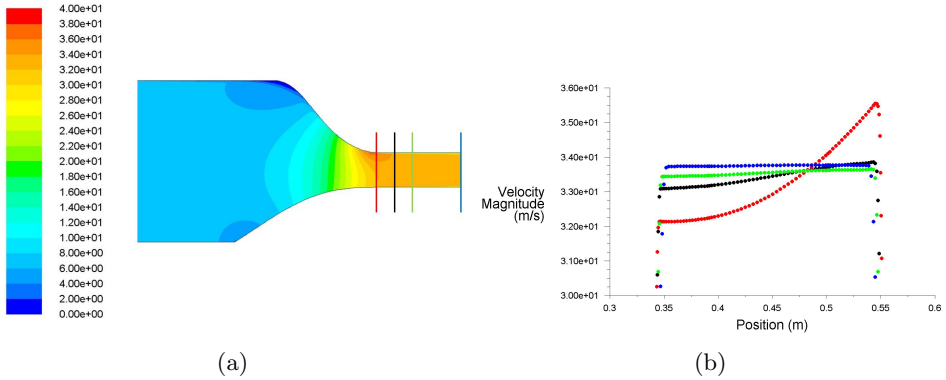


Figure 2.10: *a) Velocity contour plot of a discarded design contraction's half section. b) Velocity profile at the exit of the contraction at different positions for a discarded design.*

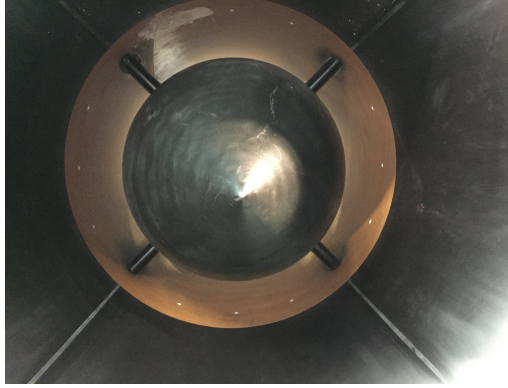


Figure 2.11: *Contraction section seen from upstream.*

Volume flow meter

Once the geometry is obtained and has fulfilled the main requirements, the contraction section is ready to be calibrated (numerically) to obtain the mass flow rate inside the LPT-OGV rig.

First, the Bernoulli equation is applied between the inlet and the outlet of the contraction section, adding a pressure loss term.

$$P_1 + \frac{1}{2}\rho u_1^2 = P_2 + \frac{1}{2}\rho u_2^2 + \frac{1}{2}K_c\rho u_1^2 \quad (2.9)$$

Here, K_c is the pressure drop coefficient and is a function of the Reynolds number. On the other hand, applying mass conservation along the contraction eq. 2.10 is obtained.

$$u_2 = u_1 \frac{A_1}{A_2} \quad (2.10)$$

Static pressures at the inlet and outlet are known since they are measured with pressure taps. Therefore, using eq. 2.9 in eq. 2.10 and making a simplification, the following is obtained.

$$u_1 = \sqrt{\frac{2(P_2 - P_1)}{\rho} \cdot \frac{1}{1 - \left(\frac{A_1}{A_2}\right)^2 - K_c}} \quad (2.11)$$

From eq. 2.11 it is easy to obtain the mass flow.

$$\dot{m} = \rho A_1 \sqrt{\frac{2(P_2 - P_1)}{\rho} \cdot \frac{1}{1 - \left(\frac{A_1}{A_2}\right)^2 - K_c}} \quad (2.12)$$

The only unknown from this equation is the pressure loss coefficient. Hence, a parametric CFD study was performed to calculate the pressure drop coefficient of the contraction section. The pressure loss coefficient calculation is obtained by simplifying eq. 2.9 as follows.

$$K_c = \frac{P_{T1} - P_{T2}}{\frac{1}{2}\rho u_1^2} \quad (2.13)$$

Here, P_T is the total pressure. The parametric study was done for mass flow values from 0.25 to 22.8 kg/s. Results of this study are shown in fig. 2.12.

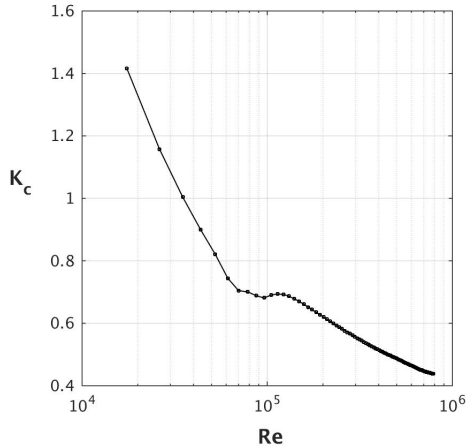


Figure 2.12: Pressure loss coefficient as a function of the Reynolds number for the final contraction section geometry.

Figure 2.12 shows that the minimum value for the pressure loss coefficient (K) inside the operational range of the LPT-OGV rig is slightly higher than 0.4 for this geometry. From the point of view of pressure losses, the losses are negligible compared with the rest

of the rig. On the other hand, the losses are not negligible for the calculation of the mass flow. If pressure losses are neglected, a 0.75% error would be inserted in the calculation according to the results of this analysis.

2.3.5 Turbine section

The turbine section is required to create realistic boundary conditions at the inlet of the EES. Figure 2.13 shows a cross section drawing of the turbine section together with the contraction and the EES.

Struts and annular screen

Downstream of the contraction section, there are two rows with four NACA 0020 profile struts. The axial chord distance of these airfoils is 300 mm, and they have a maximum thickness of 60 mm. The purposes of having these components are listed below.

- Provide access from the hub interior to the exterior to connect oil pipes to feed the hydraulic pump. A through hole of 40 mm provides enough clearance for the pipes. Moreover, there are empty holes that could be used in the future to study the effects of purge flow coming from the hub at the inlet of the rotor.
- Connect the internal to the external structure. They are the only support between interior and exterior structures, and they are, therefore, manufactured as solid steel. The struts must be stiff enough to withstand all the load without suffering large deformations. Also, these struts should have the lowest negative impact on the flow uniformity, which is a limitation to the size of the struts. Furthermore, FEA was run on the internal structure to check if it can withstand the loads and for maximum deformations (see fig. 2.14). The maximum displacement in this structure is lower than 0.1 mm in any direction.

Downstream of the struts, an annular screen is located to dissipate the wakes generated by the NACA 0020 struts. The screen has been dimensioned based on results from CFD analysis. In this simulation, a 90° sector of the turbine section (without stator and rotor) is modeled. Figure 2.14 shows how the wake after the first strut is dissipated in the screen. Therefore, a screen with the same pressure drop ($K = 1.41$) as the one used in the simulation was selected (cell width of 2 mm, wire diameter of 1 mm).

Braking system

A hydraulic brake system controls the turbine rotational speed. A hydraulic pump connected to the rotor disk through its shaft generates the torque required to control the speed. The oil is then pressurized from 1 to a maximum of 350 bar. This pressurized oil passes through needle valves that restrict and regulate the flow. The mechanical power losses in the pressure system are transformed to heat power which is dissipated through an oil-water heat exchanger connected to a water based cooling system. This brake system is meant to work up to on-design rotational speed and torque conditions (see table 2.3) and off-design cases where the higher load is transferred to the rotor shaft.

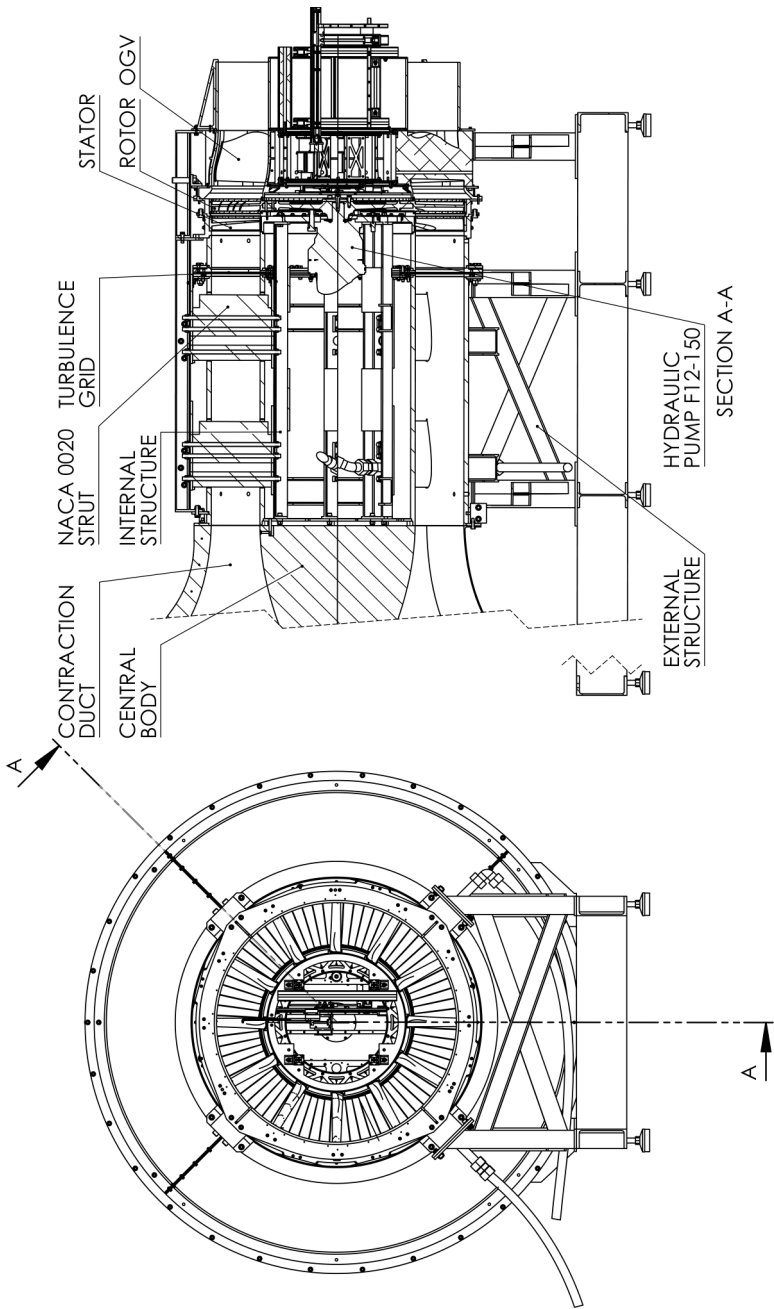


Figure 2.13: *Drawing of the turbine section.*

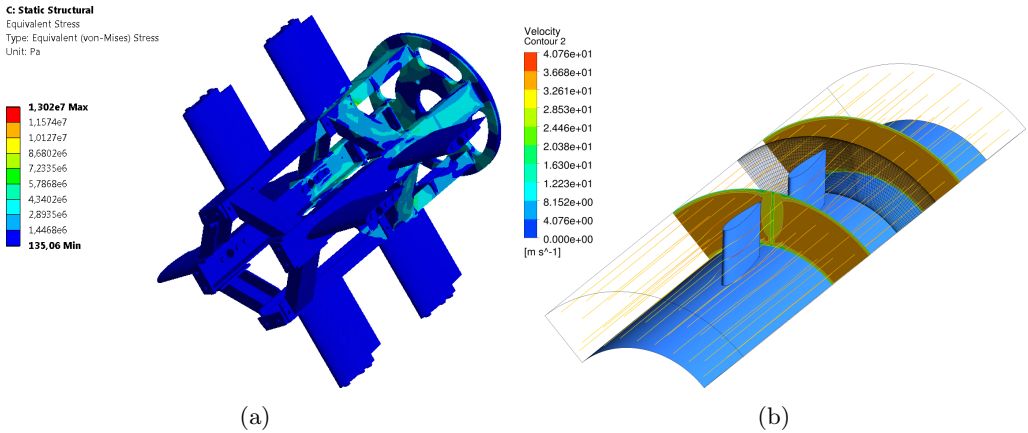


Figure 2.14: a) Stress distribution from FEA of the internal structure together with the struts. b) CFD analysis of the turbine section without stator and rotor.

There are other possibilities for controlling the rotational speed of the turbine and transferring load to the shaft. Electric generators are most common for this purpose in these kinds of facilities, but there are several advantages to having a hydraulic system. First, a hydraulic pump is more compact. Since the hub inner radius is about 320 mm, the size of the equipment is an important constraint. In addition, a hydraulic pump is simpler to install than an electric generator because there is no need for dimensioning bearings or having a stiffer structure that can stand the heavy weight of the electric equipment (77 kg [20] vs. more than 1000 kg [21]). Furthermore, the price of this electric equipment is higher than the hydraulic system. On the other hand, regulating speed and torque is more accurate using an electric generator, and there is the possibility of transferring the energy generated by the turbine to the centrifugal fan, thereby giving a more energy-efficient facility.

Turbine stage

The turbine stage is the source of realistic boundary conditions to the EES test section where aero and heat transfer measurements will be performed in the future. Table 2.3 summarizes the main parameters of this turbine stage. The Reynolds number at on-design conditions is representative of a compromise case between large turbofan engines and geared engines.

In a real engine, the flow into the EES is characterized by the swirl velocity coming from the rotor, wakes generated by the stator and rotor, tip leakage flow and purge flow coming from the hub. Hence, not only LPT dimensionless parameters should be representative of real engines but also the geometric features such as P-flange pocket, tip seal, and purge flow through rim seals. Figure 2.15 shows a detailed view where these features can be seen.

Table 2.3: Turbine stage parameters for on design conditions.

Parameter	Value
Re number based on channel height	465,000
Shroud radius [m]	0.553
Hub radius [m]	0.34
Axial velocity [m/s]	31.7
Mass flow rate [kg/s]	23.55
Inlet temperature [K]	291
Flow coefficient (Ca/U)	0.622
Load coefficient ($\Delta H/U^2$)	1.153
Rotor exit flow angle	-16.4°
Pressure ratio	1.041
Number of NGVs	60
Number of rotor blades	72
Rotational speed [rpm]	1088
Torque [N.m]	616.7
Power [kW]	70.3

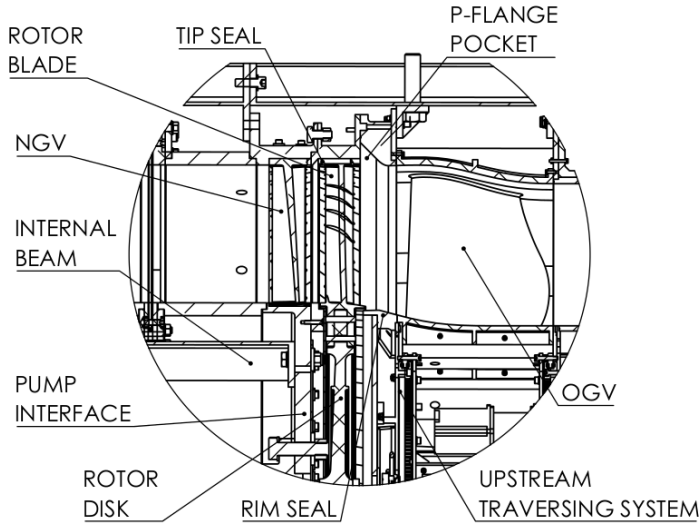


Figure 2.15: Detailed view of the turbine stage cross section.

Aero design of the turbine stage

The LPT aero design was done at GKN Aerospace Sweden. Stator and rotor blades were designed using 3-D methods, rendering complex geometries. Figure 2.16 shows a 3-D image of these components. There are 60 NGVs and 72 rotor blades in the turbine stage and 12 OGVs in the EES. The purpose of having this combination is to perform CFD

analysis of the full turbine stage together with the EES using periodic boundary conditions over a 30° sector (five NGVs, six rotor blades and one OGV). The computational time required for any CFD analysis is, therefore, significantly decreased.

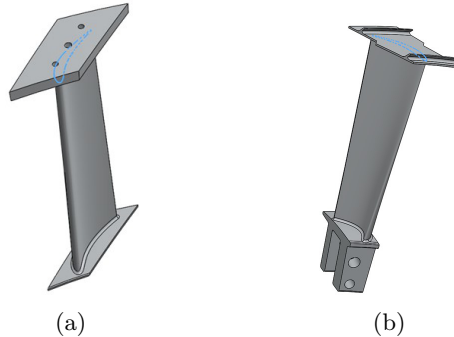


Figure 2.16: *a) NGV 3-D view. b) Rotor blade 3-D view.*

Furthermore, a tip seal was designed to obtain a realistic mass flow leakage over the rotor stage. Tip leakage flows influence flow on the EES creating rolling vortices on the surface of the vanes located at the outlet of a turbine (see Rojo et al. [22]) and considerably increase the heat transfer rate.

For the design of the tip seal, the main requirement is to obtain a mass flow leakage between 0.5% and 1% of the total mass flow coming to the turbine stage. Furthermore, since the turbine must be engine like, the tip seal design should be similar to the existing one in aero engines. CFD tools were used to design this seal. A 2D axisymmetric design process was followed under the next assumptions:

- The flow exits the stator with the same swirl angle as the NGV's outlet angle.
- The rotor does not affect the flow at the inlet to the tip sealing. Therefore, fixing a given pressure drop representative of on design operating conditions is sufficient enough to provide realistic boundary conditions.

Figure 2.17 shows the pressure distribution together with the boundary conditions applied. For the geometry parametrization, ANSYS Workbench was used as a meshing tool and the 2D axisymmetric simulations (including swirl flow) were performed in FLUENT. The turbulence model used was $k - \omega SST$ and the low Reynolds wall treatment since $y^+ < 1$.

The first conclusion drawn from this analysis was that adding more ribs does not necessarily improve the sealing performance. Figure 2.18 shows the comparison between two designs with two and three ribs, respectively. Different flow patterns were found for the two rib seal case, changing the tip seal to shroud distance as shown in Fig. 2.19. There is no such change in the flow in the three rib seal(see Fig. 2.20). The last conclusion was that the flow from the rotor does not create a major recirculation at the outlet of the tip seal.

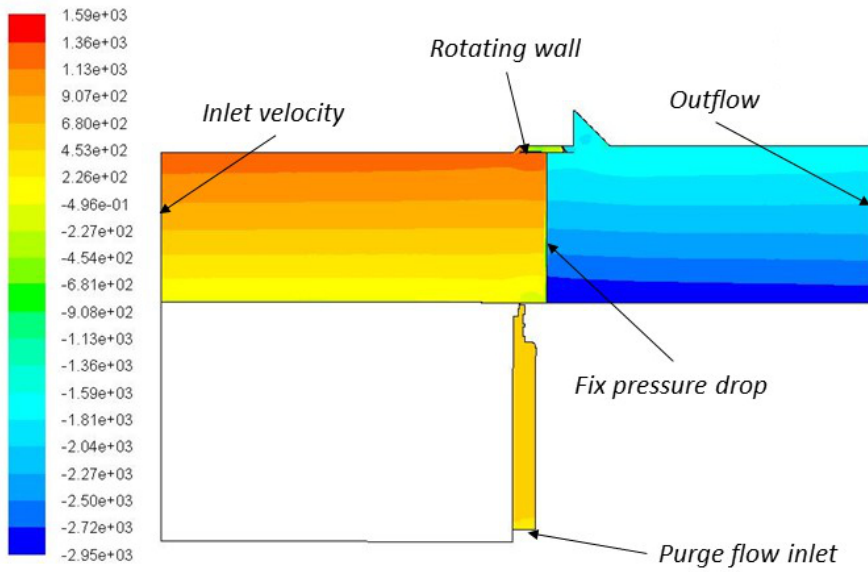


Figure 2.17: Pressure distribution for the 1.5 mm tip to shroud maximum gap case.

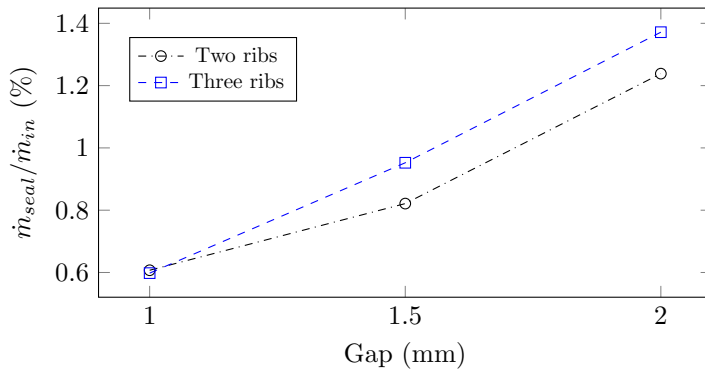


Figure 2.18: Comparison of two designs based on the mass flow ratio between the mass flow that goes through the sealing and the total mass flow at the inlet.

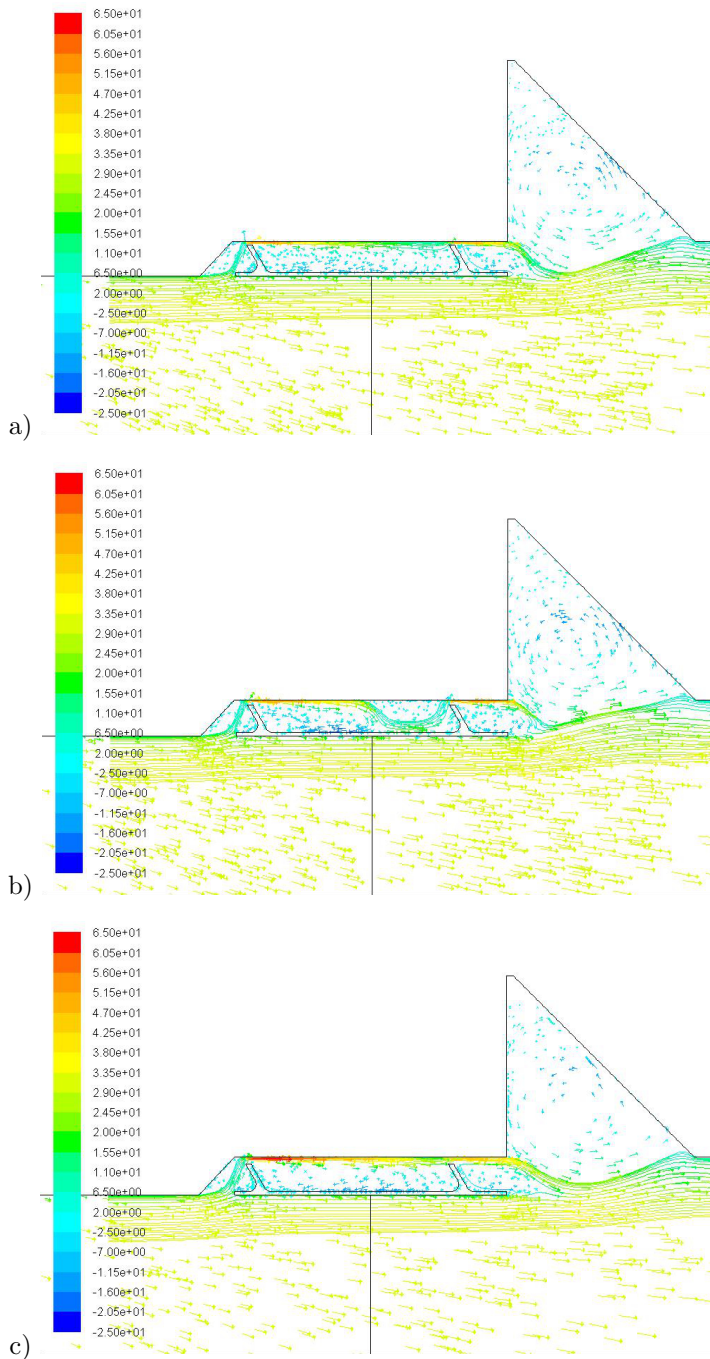


Figure 2.19: Tip seal design with two ribs. Path lines and vector velocity plot colored by axial velocity (in m/s) for tip to shroud distances of a) 1 mm, b) 1.5 mm and c) 2 mm.

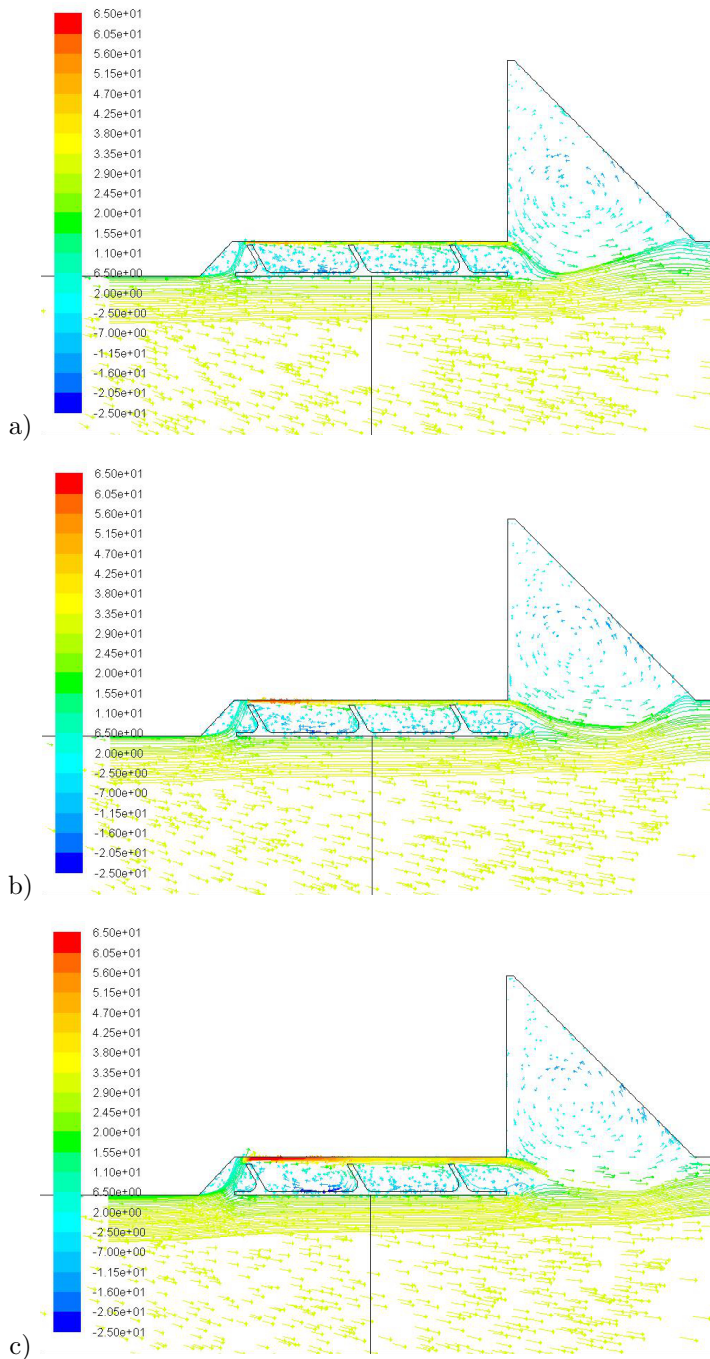


Figure 2.20: Tip seal design with three ribs. Path lines and vector velocity plot colored by axial velocity (in m/s) for tip to shroud distances of a) 1 mm, b) 1.5 mm and c) 2 mm.

Mechanical design of the turbine stage

Designing a rotating turbine requires an analysis of the loads transported from the fluid to the solid rotor. It is important to understand the main hazards for the rotor's integrity and operational stability. The most representative failure modes are listed below.

- **Static loads:** The action of aero loads on the rotor blade, fasteners, and disk could lead to blades exiting the turbine section or disk burst. For this reason, static analysis was performed.
- **Thermal load:** Creep and changes in geometry due to thermal loads can lead to contacts between the rotor and the surroundings, high local stresses, or degradation of the material's mechanical properties. The turbine operates at room temperature or slightly higher. The maximum temperature will be at the rotor shaft, where it is expected to be about 60°C. Hence, there is no need to include this load in the mechanical study.
- **Vibrations.** Most of the loads applied to the rotor have an unsteady component. This unsteady load could lead to excitation of the rotor or the structure and, in the worst case, a break-down of the turbine section. Modal analysis has been carried out in order to detect dangerous excitation modes and, if required, modify structural components to avoid operating the turbine near those modes.
- **Fatigue.** Mechanical properties of some materials change dramatically when the loads applied are cyclic. For example, since the turbine rotates at approximately 1000 rpm, during one run of five hours, $3 \cdot 10^5$ load cycles are applied to the rotor. HCF and LCF studies have been done to find a way to avoid this failure mode.

Regarding the source of loads, the most important loads are the aero loads, which act mainly in the tangential and axial directions, and the centrifugal load which is applied in the radial direction. Even though the loads could be simplified into a combination of these loads, the geometry is highly three-dimensional. Therefore, structural FEA must be performed to obtain realistic stresses and deformations over the turbine blade. Figure 2.21 shows a 5° rotor sector FEA at on-design conditions.

Furthermore, a modal analysis was made to obtain the first ten resonance frequencies of the rotor. Afterwards, with knowledge of these frequencies and the main excitation sources, a Campbell diagram was constructed to assess potential resonance vibration problems. Figure 2.22 shows the diagram. Structural and modal analysis were carried out using commercial software ANSYS Workbench.

Note that the resonance frequency for nodal diameters larger twelve converge to the same value, which is approximately the same as the resonance frequency of a single blade.

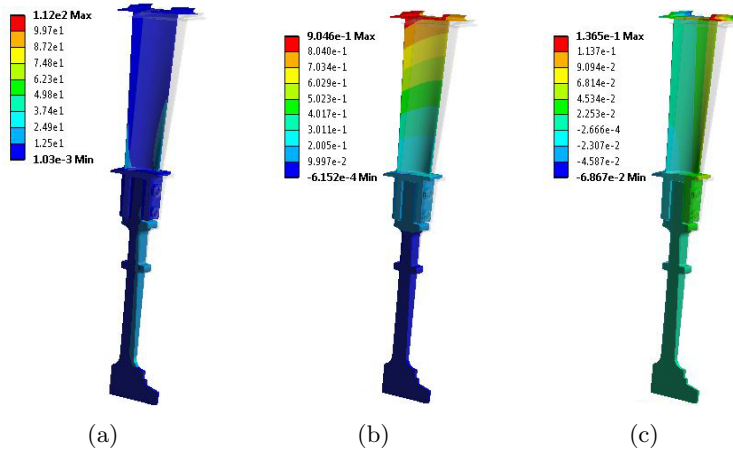


Figure 2.21: Results of static stress FEA analysis of 5° rotor sector at on-design conditions. a) Stress distribution (in MPa), b) axial displacement (in mm) and c) radial displacement (in mm). Deformation scale factor of the deformed geometry is 31.

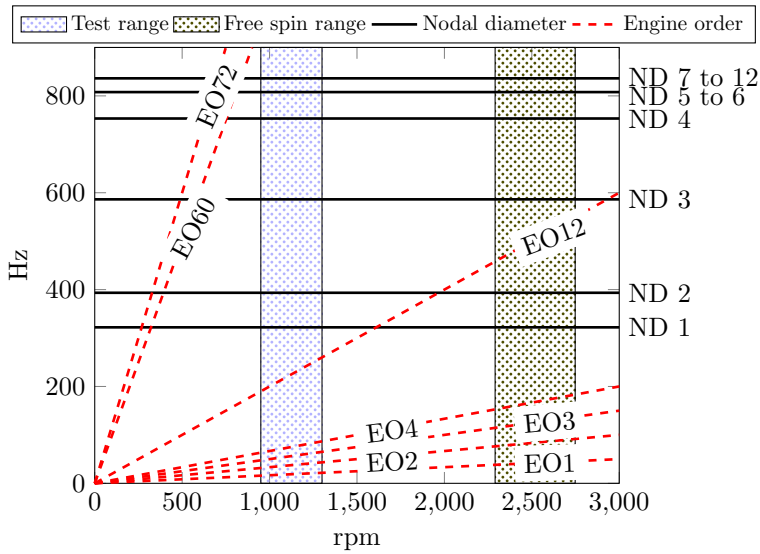


Figure 2.22: Campbell diagram of the rotor turbine.

2.3.6 Engine exit structure

The aero design of the EES was done at GKN Aerospace Sweden using an in-house code. Mechanical design of this component was done at Chalmers. Figure 2.23 shows a 3-D view of this component.

There are twelve OGVs in the EES, comprising ten aluminum machined pieces and two 3-D printed OGVs instrumented with pressure taps. A cavity engine-like for purge flow injection is included in the design. A realistic P-flange pocket is located downstream of the LPT rotor shroud. Two traversing systems are located inside the EES hub. The upstream traversing system rotates together with the rim seal, enabling 360° measurements and can traverse radially through all the annulus. The downstream traversing system rotates the outlet hub of the EES, enabling 360° measurements and can traverse radially and axially. The downstream traversing system can be used to study several planes inside the EES. Both traversing systems can be instrumented with multi-hole probes as shown in fig. 2.23 or other measurement devices such as hot wires.

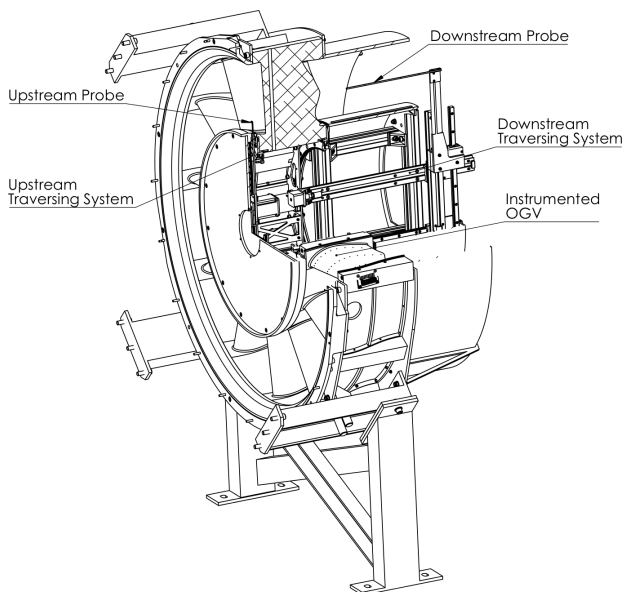


Figure 2.23: *Half-section of the EES.*

This modular design allows for the quick change of individual or all OGVs, P-flange pocket, or rim seal. Also, purge flow can be inserted through the end-cap located in the center

Moreover, this component has a practical use in this facility since it is designed to remove the swirl coming from the LPT and, therefore, obtain axial flow at the outlet.

2.4 Pressure drop calculation

The design of these kinds of facilities requires a continuous design loop where one of the most important parameters to take into consideration is the total pressure drop in the facility. For this facility (and most low-speed wind tunnels), there is a trade-off between reaching the highest Reynolds number possible in the test section and the size of the

facility and power of the motor unit that drives the flow. In this case, the limitations are 200 kW of electric and cooling power supply and the space available in the lab (7 m height, 4 m width and 14 m length). Once the turbine parameters are set, the Reynolds number in the test section and the mass flow rate are known. When previous limitations are taken into consideration, one can start calculating the pressure distribution for different rig concepts.

Empirical correlations and/or CFD tools were used to calculate the pressure drop for each component. These empirical correlations are summarized in Barlow et al. [13]. Also, pressure measurements were performed in the flow conditioning of a similar annular-cascade rotating rig at Chalmers University of Technology (see Arroyo et al. [23]). In these data, correlations were obtained for the pressure drop coefficient of turbulence screens, as shown in fig. 2.24. These correlations showed a larger pressure drop coefficient compared to what would be expected from older correlations. An explanation for this anomaly could be that dust had accumulated in the screens (especially over finer screens) and honeycomb.

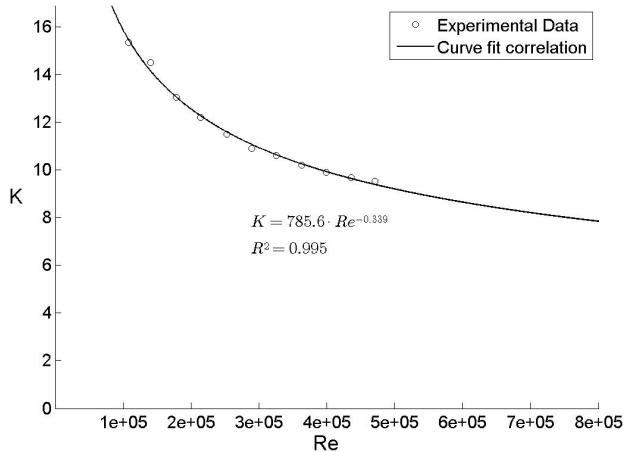


Figure 2.24: Measured pressure drop coefficient for a turbulence screen. Wire diameter and cell width of 0.33 and 1.25 mm respectively.

There are two main outcomes of this analysis regarding the sizing of the rig and the location of different components. First, the heat exchanger should be located where there is the largest cross section area because the losses are proportional to the square velocity, and the pressure drop coefficient is the highest in the entire facility. The second outcome is that the size of the flow conditioning ducts should be at least 2 m in diameter to produce less than 10% losses in this section. However, in order to minimize pressure losses in the diffusing section, a long diffusing section is designed in order to avoid placing a turbulence screen inside the diffusing section. Figure 2.25 shows the main sources of pressure loss inside the rig.

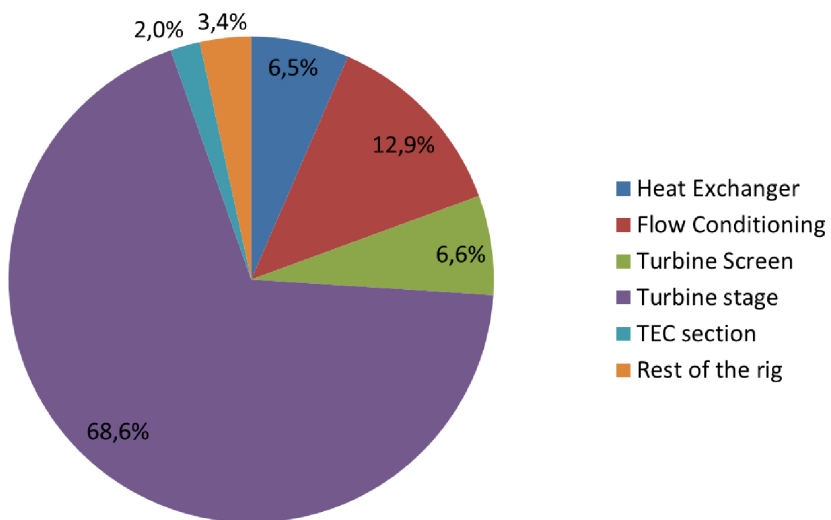


Figure 2.25: *Pressure budget of the facility.*

3 Aerodynamic Measurements Setup

This chapter describes the experimental setup of the LPT-OGV facility. It includes a description of the measurement system and techniques, as well as error estimation for each measurement technique. This error estimation provides good insight for understanding the limitations of pressure-measurement techniques used during the test campaign.

3.1 Experimental layout

Experimental data discussed in this thesis are acquired by means of the experimental setup shown in fig. 3.1. Two PCs run simultaneously to control the facility and the measurement system. The facility is controlled by regulating the rotating speed of the centrifugal fan and the LPT braking torque by means of a set of valves in the hydraulic brake system. The “Control PC,” which shares data real-time with the “Main PC,” controls these components. The “Main PC” controls both traversing systems and data acquisition systems for aero measurements. All monitoring and aero measurement data are stored in the Main PC. Both PCs are controlled remotely. Figure 3.2 shows an schematic of the test section.

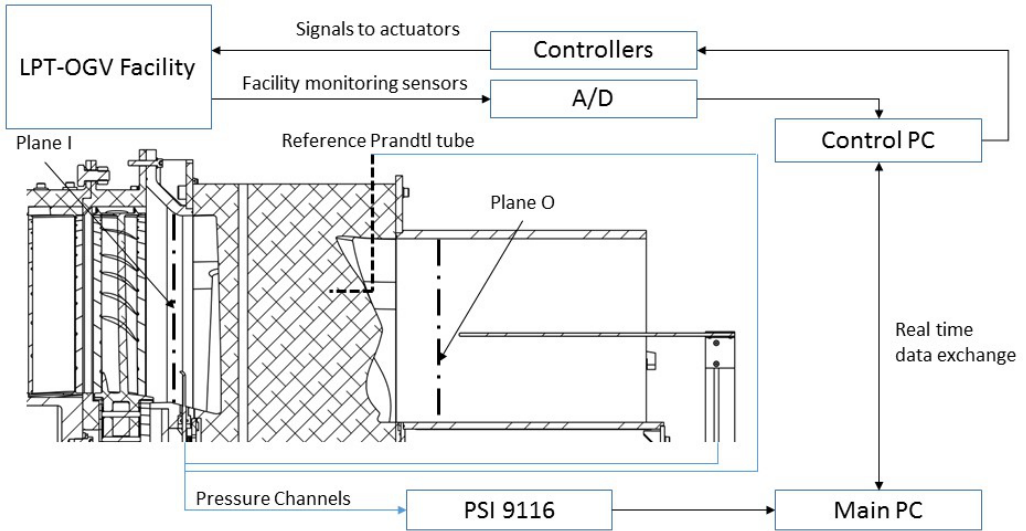


Figure 3.1: *LPT-OGV acquisition and control system setup.*

To measure the mass flow in this facility, an accurate manometer (model FCO510 from Furness Controls) measures the static pressure difference between the inlet to the outlet of the contraction section and, from eq. 2.12, computes the mass flow through the LPT and test section. Furthermore, a 16-channel digital pressure scanner (model PSI 9116 from Pressure Systems, Inc.) measures the relative pressure with respect to room pressure

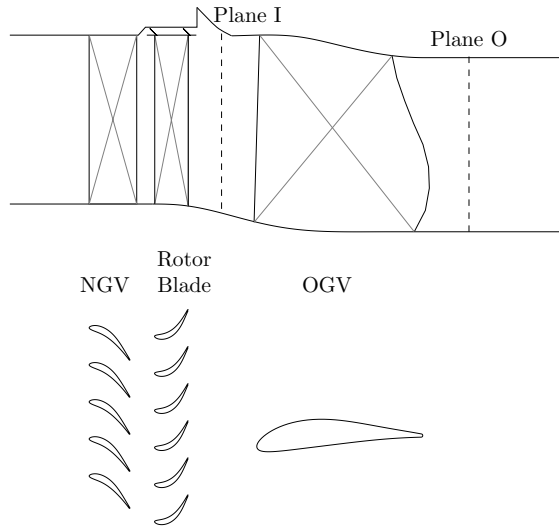


Figure 3.2: *Schematic of the test section*

from pneumatic channels. Twelve channels are dedicated to the multi-hole probes, two channels to the Prandtl tube, and one channel is connected to three Scanivalve pressure multiplexers (not simultaneously). The EES pressure taps are connected to these pressure multiplexers. See fig. 3.3. Note that a reference Prandtl tube is used to obtain static and total pressure distributions.

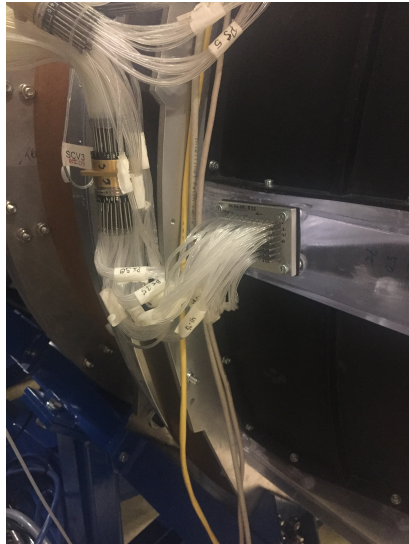


Figure 3.3: *Pressure taps interface plate.*

3.2 Multi-hole probe

Flow inside an EES is known to be highly 3-dimensional, containing secondary flows, wakes, and other complex flow features. Therefore, a multi-hole probe is required in order to characterize the flow at several planes. Other measurement techniques such as Particle Image Velocimetry (PIV) and Laser Doppler Anemometry (LDA) are also suitable to measure velocity distributions of complex flow fields. An L-shaped five-hole probe is located upstream from the OGV, facing the incoming flow, and turned about 16° with respect to the axial direction. A straight seven-hole probe located at Plane O faces the flow parallel to the axial direction. The five-hole and seven-hole probes are 1.2 and 1.6 mm in diameter respectively. Both probes are calibrated at Chalmers using AeroProbe calibration protocols.

3.2.1 Uncertainty Estimation Multi-hole Probe

Five-hole and seven-hole probes have the same sources of errors in our test section since they are working under the same physical principle and are connected to the same pressure systems. For each probe, points which are representative of the measured flow are chosen to determine the percentage of error for each variable. Two points located near the tip and mid-span of Plane I are selected to estimate the errors on the five-hole probe. For the seven-hole probe, one point is in the bulk flow region at Plane O. A similar procedure was done by Axelsson [24] to estimate the errors from multi-hole probes.

Figure 3.4 shows the results from a study on the time response of the total pressure. The outcome of this study is the sampling time which will be used in all experiments. The author has decided that a sampling time of 3s is enough for our measurements since the error on the total pressure ensemble average is lower than 0.4% in all cases. Furthermore, 3s sampling time allows to perform one ADP case measuring Plane I and Plane O in 8 hours.

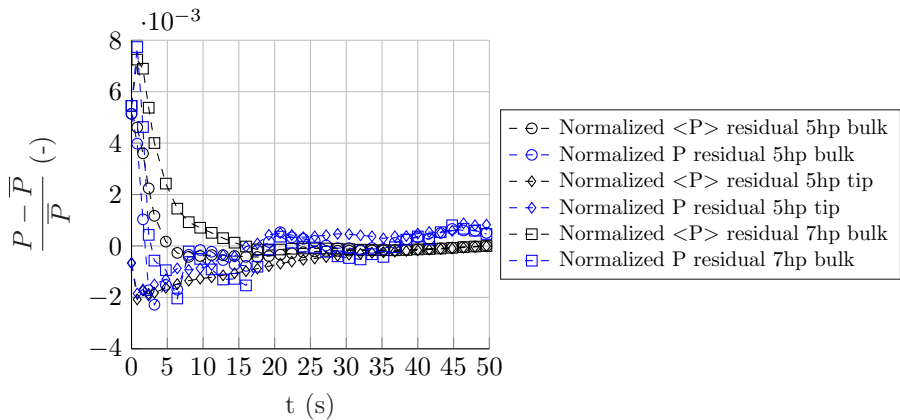


Figure 3.4: *Influence of sampling time on total pressure error.*

Uncertainty from probes alignment

The alignment of the upstream probe is performed by locating an air jet stream parallel to the axial axis upstream of the 5hp. Then, the relative angle between the 5hp and the jet is measured using the readings from a PSI unit, obtaining that the probe is facing the flow coming from the LPT at -15° . Looking at table 3.2, the error in cone angle is approximately 0.88° . Afterwards, the rig is run at ADP conditions and measurements are performed with both probes at several locations of Plane I to check the alignment of both probes. The result from this experiment is that all measures are inside the error ranges, and, therefore, the author assumes that the alignment error of the 7hp is 0.45° . These bias errors are added in subsection 3.2.1.

Uncertainty from pressure measurement unit

From the pressure measurement unit, PSI 9116, a bias and random error sources are estimated. The bias error corresponds to the ± 2 Pa accuracy from our in-house calibration protocol of this unit. Figure. 3.5 shows the measured error of the PSI 9116 unit after calibration.

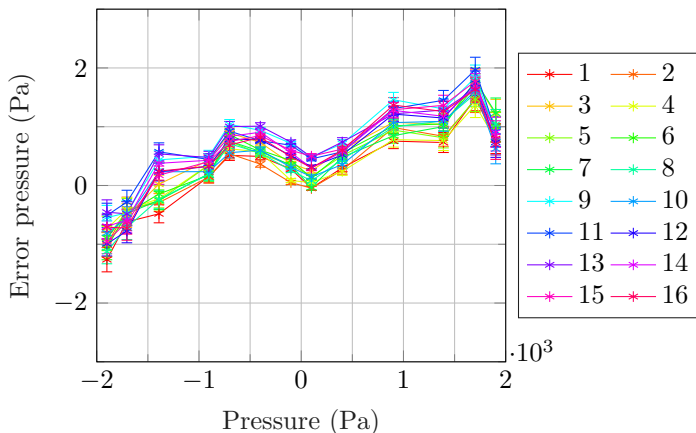


Figure 3.5: *PSI 9116 channels error*

To calibrate the PSI 9116, all PSI channels are compared over different reference pressures against readings from a FCO unit. FCO's accuracy stated by the manufacturer's calibration protocol is $\pm 0.01\%$ over the reading pressing inside our pressure range. The random error S_k is calculated from the number of samples and the corrected standard deviation s of N independent samples. Equation 3.1 shows how this error is calculated.

$$S_k = t_{\alpha/2, n-1} \cdot \frac{s}{\sqrt{N}} \quad (3.1)$$

Where $t_{\alpha/2, n-1}$ is the t-Student distribution coverage factor for a confidence interval of 95% and $n - 1$ degrees of freedom. Note that the t-Student distribution converges to a

Table 3.1: Absolute error for all variables from pressure measurement unit, PSI 9116. All values are represented in SI units.

	ϵ_{P_t}	ϵ_{P_s}	ϵ_{v_x}	ϵ_{v_r}	ϵ_{v_θ}	$\epsilon_{C_{p_0}}$	ϵ_{C_p}	ϵ_α	ϵ_β
5hp Bulk	2.69	4.95	0.177	0.118	0.127	0.0038	0.007	0.173	0.23
5hp Tip	3.15	4.66	0.146	0.079	0.148	0.0044	0.0065	0.241	0.141
7hp Bulk	2.49	5.47	0.181	0.09	0.103	0.0034	0.0076	0.165	0.152

Gaussian distribution when the number of independent samples is larger than 30.

Then, the absolute error from an independent variable x or, in this case, the pressure reading of each channel can be estimated as a combination of statistical and bias errors as shown in Eq. 3.2.

$$\epsilon_x = \sqrt{\sum_{i=1}^n S_i(x)^2 + \sum_{j=1}^m B_j(x)^2} \quad (3.2)$$

In this equation, n and m are the number of statistical and bias errors respectively. Therefore, once the absolute error of each pressure channel is calculated, the error from the PSI on each variable is estimated by a permutation of the measured pressures, adding or subtracting the calculated absolute error. In the case of the five-hole and seven-hole probes, the number of the permutations are 2^5 and 2^7 respectively. The largest error for each variable from comparing the averaged value to the permuted values is selected. Table 3.1 shows a summary of errors generated by pressure measurement uncertainties in each measured variable.

Uncertainty from Probe

Both five-hole and seven-hole probes were calibrated at Chalmers by means of an automated traversing system located downstream from an axial air jet at ambient conditions. The traversing system can rotate the probes around their axial and radial axis, modifying the relative cone angle and roll angle between the probe and the jet stream. The quantities measured to calibrate the probes are listed below.

- The dynamic reference pressure for the calibration protocol was measured by an FCO unit. Device accuracy has been used as bias error source, $\pm 0.01\%$.
- The static reference pressure for the calibration protocol was measured by a PSI 9116 unit. Device accuracy has been used as the bias error source, $\pm 2 Pa$.
- The channel pressures for the multi-hole probe were measured by a PSI 9116 unit. Device accuracy has been used as the bias error source, $\pm 2 Pa$.

Table 3.2: Error from calibration protocol for different conical angles. Note that dynamic and total pressures values are around 800 Pa during calibration.

Conical angle, deg	5hp			7hp		
	<15	<30	<45	<15	<30	<45
ϵ_{P_t} (%)	0.526	0.539	0.646	0.409	0.705	1.032
ϵ_{P_d} (%)	0.575	0.729	1.31	0.374	3.518	3.518
ϵ_α (°)	0.829	0.880	3.12	0.449	1.129	6.952
ϵ_β (°)	0.876	0.876	0.876	0.401	1.430	3.295

- The relative angles between the probe and the jet stream were measured by an encoder located in each of the DC motors. Alignment estimated accuracy has been used as bias error source, $\pm 0.3^\circ$.

The data obtained for calibration is post-processed in an aero-probe executable that using local least squares method and few pressure coefficients fit the n-hole pressure signals returning all pressures and relative velocities. Furthermore, the total pressure during calibration from the stream jet was approximately 800 Pa, representative of the maximum total pressure inside the test section. The Reynolds number based on probe diameter was 40k. Table 3.2 shows the most significant errors obtained from this calibration process. Note that in the current experimental layout, the seven-hole probe relative conical angle to the flow is, at most measurement locations, lower than 15° . Moreover, the five-hole probe conical angle is lower than 15° in approximately 60% of the measurement locations, but lower than 30° in the rest. The variables listed in table 3.2 are used as independent variables to calculate all variables of interest by means of error propagation. The error of a dependent variable, R, is calculated as shown in eq. 3.3.

$$\delta R(x_1, \dots, x_n) = \left\{ \sum_{i=1}^n \left(\frac{\partial R}{\partial x_i} \cdot \delta x_i \right)^2 \right\}^{1/2} \quad (3.3)$$

Here, n is the number of independent variables, x_i an independent variable, and δx_i its absolute error. In this case, the selected independent variables are the total pressure, dynamic pressure, swirl angle, and yaw angle. The errors from the calibration procedure are summarized in table 3.3.

Summary errors

Table 3.4 shows a summary of all errors. These values were obtained by applying the root mean squared sum of all values from tables 3.1 and 3.3. An interesting fact from looking at table 3.4 is that relative errors are not always good indicators of accuracy. For

Table 3.3: Absolute error for all variables from probe calibration. All values are represented in SI units.

	ϵ_{P_t}	ϵ_{P_s}	ϵ_{v_x}	ϵ_{v_r}	ϵ_{v_θ}	$\epsilon_{C_{p0}}$	ϵ_{C_p}	ϵ_α	ϵ_β
5hp Bulk	3.30	4.78	0.195	0.69	0.651	0.00543	0.00716	1.21	1.24
5hp Tip	4.37	5.98	0.114	0.747	0.727	0.0072	0.00865	1.21	1.24
7hp Bulk	2.67	3.95	0.166	0.622	0.590	0.00473	0.00628	0.988	0.967

example, the swirl and yaw angle errors for the seven-hole probe bulk region case are similar in absolute terms but in relative terms, the swirl angle relative error is almost four times worse than the yaw angle relative error

Furthermore, an interesting outcome of this study is the impact of the different error sources on each variable. Figure 3.6 shows the impact of each error source over the absolute error of each measured quantity. It is interesting that the uncertainty of the probe calibration and alignment has a similar impact over the pressure-based variables as the uncertainty from the pressure measurement unit. On the other hand, all velocity component errors are strongly correlated to the probe alignment and calibration protocol uncertainties.

Table 3.4: Summary table of multi-hole probe errors. Absolute errors are shown in SI units.

	5hp Bulk		5hp Tip		7hp Bulk	
	Absolute	Relative %	Absolute	Relative %	Absolute	Relative %
ϵ_{P_t}	4.25	0.678	5.39	0.648	3.65	0.559
ϵ_{P_s}	6.89	37.4	7.58	6.50	6.75	5.17
ϵ_{v_x}	0.263	0.854	0.185	0.538	0.246	0.682
ϵ_{v_r}	0.700	44.0	0.752	35.1	0.628	41.9
ϵ_{v_θ}	0.663	8.22	0.742	50.9	0.599	142
$\epsilon_{C_{p0}}$	0.0066	65.1	0.0084	3.05	0.0058	29.4
ϵ_{C_p}	0.0100	7.40	0.0108	3.93	0.0098	15.6
ϵ_α	1.22	8.33	1.23	50.9	1.00	149
ϵ_β	1.26	42.7	1.25	35.1	0.979	41.1

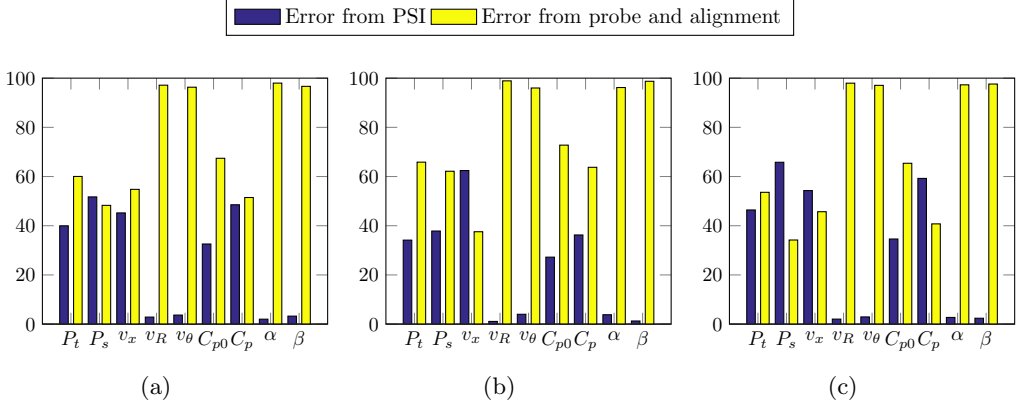


Figure 3.6: *Percentage error contribution to absolute error from pressure measurement unit and probe error sources at (a) 5hp bulk region, (b) 5hp tip region and (c) 7hp bulk region. The alignment error source is included in the probe error source since this error is added directly on the swirl and yaw angle uncertainties from the probe.*

3.3 Pressure taps

To measure the static pressure distribution over the OGVs, instrumented 3-D printed OGVs were designed with pressure taps. Figure 3.8 shows a manufactured prototype. Two OGVs with 20 pressure taps at 12.5, 50, 87.5, and 25, 50, 75% span respectively, are located inside the EES. Furthermore, each one of them has nine pressure taps at 5% span the pressure side and the suction side. All geometries were manufactured using the stereolithography (SLA) additive manufacturing technique. The hole diameter of the taps and connecting tubes are 1.2 and 1.8 mm respectively.

The design process of this component starts by comparing results from preliminary CFD simulations of each design point with what would be obtained if only twenty pressure taps were located in each span. Iteratively, a set of locations for each pressure tap produces an error lower than 2% in blade loading comparing to CFD (except for the 5% span taps, those are located uniformly distributed). Afterwards, a Python script that generates Solidworks macros (in Visual Basic) generated the pressure taps and channels, organizing them in a rectangular pattern. Figure 3.7 shows a 3-D printed OGV CAD design. It takes about 2 hours, from an OGV CAD and the pressure tap locations, to obtain a new geometry ready for 3-D printing.

Geometry tolerances errors from SLA manufacturing technique have been measured manually using a ROMER measurement arm. The geometry deviates +0.45% and -0.55% from nominal maximum length and width while the local error of each profile is lower. The manufacturer stated a tolerance of ± 0.25 mm in x and y direction (both perpendicular to the radial direction) and ± 0.4 mm in radial direction. Due to these tolerances, the author decided that all channel diameters must be at least twice the largest tolerance error to avoid particle deposition inside the channels and clogging.

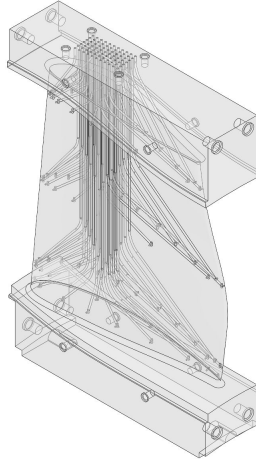


Figure 3.7: 3D view of OGV CAD model.



(a)



(b)

Figure 3.8: (a) Photo of a 3-D printed OGV used for static pressure measurements. (b) Detail view of the OGV 3-D printed at the trailing edge.

3.3.1 Uncertainty Estimation Pressure Taps

To estimate the errors, Tropea et. al. [25] shows a summary of different error sources to consider¹. One of the main error sources is the alignment of the tap, as it should be normal to the surface. In the current case, the hole's alignment is dependent only on the SLA accuracy. There are also pressure corrections as a function of the tap geometry and wall shear stress, but since wall shear stress at those locations is unknown, and the OGV's tap topology differs from a straight tap, the author does not apply corrections for these features. However, doing a rough estimate assuming the geometry of the channels

¹The author strongly recommends to check this book before starting the design of any new experiment inside fluid mechanics' field.

behaves as a straight pressure tap and making use of wall shear stress calculated by CFD simulations, the pressure correction could reach -23.7 Pa.

On the other hand, errors from the pressure measurement units are accounted for. The experiments were performed using a sampling time of 3s and a settling time of 1s. Figure 3.9 a) shows an example of static pressure and static pressure coefficient distribution (see eq. 4.5) of two OGVs' 50% span including error estimation. Figure 3.9 b) indicates a correlation between the static pressure coefficient and its absolute error. This trend is a consequence of the static pressure coefficient's definition because absolute error sources do not correlate with the static pressure coefficient.

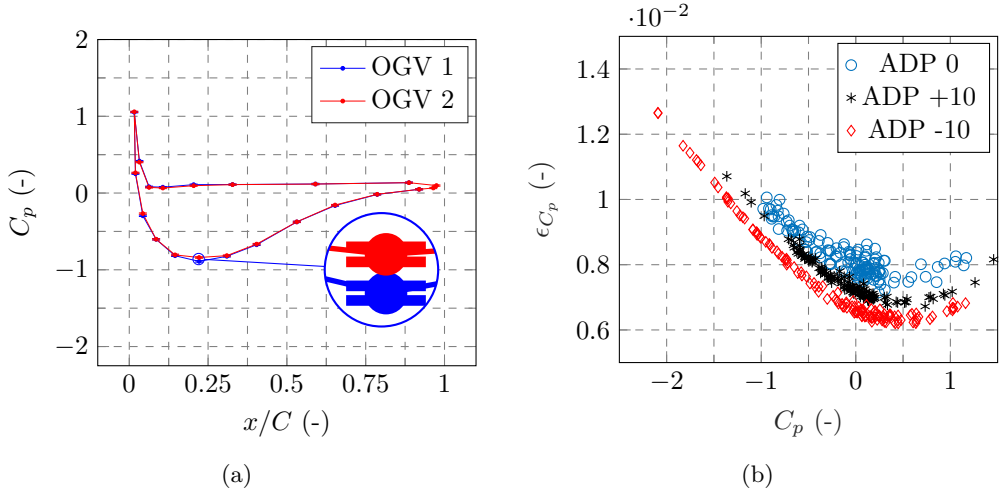


Figure 3.9: (a) Static pressure coefficient error bar at 50% span of two different OGVs at ADP 0. (b) Absolute error as function of the static pressure coefficient from all pressure taps at all design points.

3.4 Notes on Heat Transfer Experiments

Despite of not performing heat transfer experiments inside the EES, the author considers worth describing briefly the theoretical background of heat transfer measurements performed during his PhD in other facilities where similar flow physics are present.

In order to measure heat transfer, a simplified model shown in Fig. 3.10 describes the heat transfer mechanisms involved. The experiment consist of one solid with low thermal conductivity which is exposed to the gas path on one side, where the temperature is measured by an IR-camera, and other side that is heated by a hot water stream as in Arroyo [11] or by an aluminium core which contains electric heaters as in Rojo [22] and Rojo [9]. Knowing the thickness of the solid, temperatures on both sides and the thermal conductivity, the conductive heat flux is calculated as shown in Eq. 3.4.

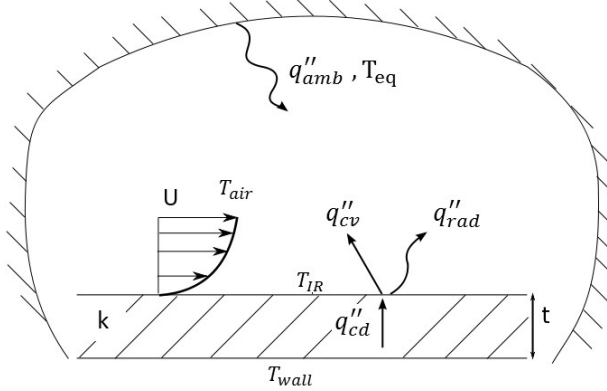


Figure 3.10: *Simplified model for heat transfer measurement.*

$$q''_{cd} = k \frac{T_{wall} - T_{IR}}{t} \quad (3.4)$$

Once is know the conductive heat flux through the insulating layer, this heat flux is dissipated into convective heat and radiative heat. In order to estimate the radiative heat transfer shown in Fig. 3.10, it is assumed that the surrounding is sufficiently large that the temperature does not change despite of the radiative heat flux generated by T_{IR} . The temperature from the background radiation, T_{eq} is assumed to be the same as the flow temperature in our experiments. In addition, there are no reflections back to the insulating solid. Hence, Eq. 3.5 can be used to calculate the radiative heat flux.

$$q''_{rad} = (\epsilon\sigma T_{IR}^4 - \sigma T_{eq}^4) \quad (3.5)$$

The expression for the convective heat transfer is known as Newton's law and is shown in Eq. 3.6 for this model.

$$q''_{cv} = h \cdot (T_{air} - T_{IR}) \quad (3.6)$$

Applying energy conservation as shown in eq. 3.7 and simplifying the expression, the convective heat transfer coefficient can be expressed as function of known or measured values. Equation 3.8 shows the expression for calculating the convective heat transfer coefficient.

$$q''_{cd} = q''_{cv} + q''_{rad} \quad (3.7)$$

$$h = \frac{k \left(\frac{T_{wall} - T_{IR}}{t} \right) - \epsilon (\sigma T_{IR}^4 - \sigma T_{eq}^4)}{T_{air} - T_{IR}} \quad (3.8)$$

Note that eq. 3.8 is only valid if there no lateral thermal conduction effects and radiative heat transfer can be simplified as shown in eq. 3.5. In reality, 3-D thermal conduction effect are taken into account. A 3-D CFD simulation of the solid insulating layer where temperatures measure by an IR-camera of the air-solid interface and by thermoresistors on the other side. Providing both Dirichlet boundary conditions and assuming adiabatic walls at any other surface boundary, accurate conductive heat flux calculations can be performed. Once conductive heat flux is calculated accounting for 3-D effects, convective heat transfer coefficient is calculated by applying same energy balance as shown in eq. 3.7.

Regarding IR-thermography measurement technique, information on non-uniformity correction, calibration and data processing is described in detail by Rojo et. al. [9] and Rojo et. al. [22].

4 Results

This chapter summarizes all results from aero measurements performed in the LPT-OGV rig. First, definitions of the most important quantities for evaluating flow characteristics are introduced. Next, results from commissioning are shown in order to determine the most important assumptions such as flow periodicity or no interaction of components located upstream of the LPT stator. This chapter continues with the results obtained from multi-hole probes and pressure taps. Flow features such as wakes, hub vortices, and shroud vortices from the stator can be visualized at different LPT running conditions. Moreover, wakes generated by the OGVs are visualized and provide an insight of the EES performance. Furthermore, the performance of the EES is evaluated quantitatively and compared with CFD predictions. Also, a comparison between numerical and experimental total pressure coefficient, static pressure coefficient and swirl angle profiles circumferential and radial profiles is performed. Finally, a comparison of static pressure coefficient distributions between CFD and experimental data is performed.

4.1 Definitions

Since results shown in this thesis are related to aerodynamic measurements, only pressure coefficients and velocity component definitions are required to characterize each case and compare experimental data with CFD. First, velocity swirl and yaw angle definitions are shown in eqs. 4.1 and 4.2 respectively.

$$\alpha = \arctan \left(\frac{V_\theta}{V_x} \right) \quad (4.1)$$

$$\beta = \arctan \left(\frac{V_r}{V_x} \right) \quad (4.2)$$

Note that α and β are commonly used for contour plot visualization instead of radial and circumferential velocities. Variables α and β are expressed in degrees. Positive values of α and β correspond to the circumferential velocity of the LPT rotational speed and radial velocity pointing outwards respectively. Another quantity which is helpful on the identification of flow features is the axial vorticity, defined in eq. 4.3.

$$\omega_x = \frac{1}{r} \left[\frac{\partial (rV_\theta)}{\partial r} - \frac{\partial V_r}{\partial \theta} \right] \quad (4.3)$$

Arroyo [11] suggests that vorticity plots together with swirl and yaw angle plots are a useful tool for the identification of vortices.

Total and static pressure coefficients are shown in eqs. 4.4 and 4.5 respectively. A Prandtl tube is installed inside the EES to measure static and total reference pressures. Dynamic reference pressure, q_{ref} , is calculated from static and total reference pressure.

This reference point was included as well in the computational domain to compare pressure coefficients.

$$C_{p_0} = \frac{P_{t,i} - P_{t,ref}}{q_{ref}} \quad (4.4)$$

$$C_p = \frac{P_i - P_{ref}}{q_{ref}} \quad (4.5)$$

The main purpose of making use of pressure from a fixed point is to reduce the error from pressure fluctuations generated by the LPT. Since the pressure drop through the LPT rotor stage is about 4000 Pa, a 0.5% fluctuation of that value is on the same order of magnitude as the pressure losses generated by the EES. Errors generated by these fluctuations are assumed to be decreased by using relative quantities.

4.2 Comissioning

Flow measurements at the outlet of the flow conditioning section and downstream of the annular turbulence screen were carried out to determine the flow velocity and temperature uniformity. To provide a numerical and not only a qualitative measure of the flow uniformity, the same expression as in Steen et. al. [26] was used. This expression is shown in eq. 4.6.

$$\sigma = \sqrt{\frac{\sum_{i=1}^n A_i (U_i - \bar{U})^2}{\sum_{i=1}^n A_i \bar{U}^2}} \quad (4.6)$$

Figure 4.1 shows the experimental data obtained using a Prandtl tube and a thermocouple attached to the Prandtl tube at the outlet of the flow conditioning section. The probe was traversed manually and was attached to a NACA 0021 profile beam 2.5 meters long and 75 millimeters thick; therefore, the accuracy of the positions plotted are estimated as 5 mm, and the experimental data were affected by the vibrations on the long and slim NACA profile. Moreover, the measurements were performed without all components located downstream of the flow conditioning's outlet.

Figure 4.2 shows the velocity distribution at the outlet of the annular turbine screen. Four wakes generated by the structural NACA 0020 struts are still measurable after the annular turbulence screen. There is another wake at approximately 30° which corresponds to a Prandtl tube which was located 300 mm upstream from the annular turbine screen and downstream the axisymmetric contraction outlet. This probe was removed after the measurements were done. Also, fig. 4.2 shows that there is not a radial or azimuthal velocity gradient except for the wakes generated by the NACA struts. Hence, the only sources of non-periodic velocity profile at the outlet of the LPT stage are the wakes generated by the NACA struts and manufacturing non-conformances of the NGVs and rotor blades.

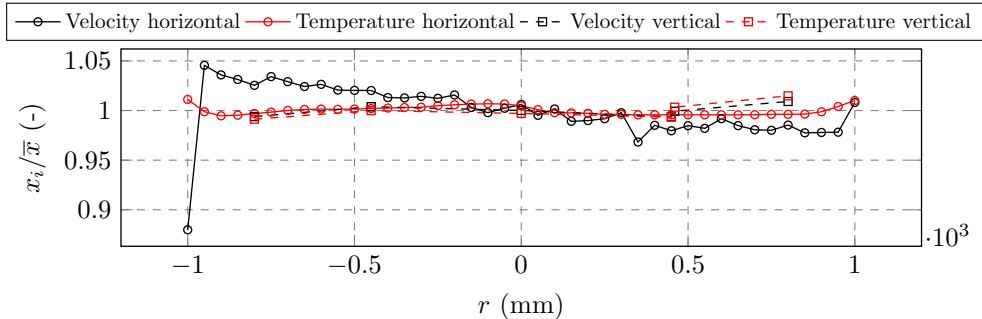


Figure 4.1: *Normalized velocity and temperature profile at the outlet of the flow conditioning. The Prandtl tube and thermocouple were traversed in horizontal and vertical direction. Flow velocity and temperature non-uniformity (σ) over the measured lines is lower than 2.8% and 0.8% respectively.*

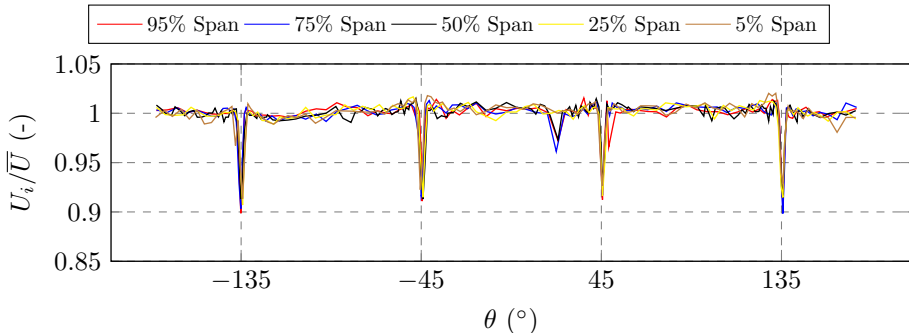


Figure 4.2: *Velocity profile at 98.5 mm upstream the LPT stator. Flow velocity non-uniformity (σ) over the measured plane of 2.2%*

Also, 360° mid-span measurements were performed at Plane I and Plane O to check periodicity inside the test section. Figures 4.3, 4.4 and 4.5 show the main results from this study. From the total pressure and velocity profiles shown in fig. 4.3, there is no indication of a 90° perturbation from the NACA 0020 struts. Looking at fig. 4.4(a) and (b), there is not a peak at 1/90 deg⁻¹ indicating the existence of wakes from the struts at Plane I or Plane O mid-span. Furthermore, eq. 4.6 is used to evaluate the non-uniformity of a superposition of all 30° sectors. The average error on total pressure and axial velocity at Plane I is 1.17% and 0.54% respectively, while at Plane O is 1.57% and 0.63%.

In fact, the most influencing component in the PSD diagram at Plane I mid-span (fig. 4.4 (a)) is generated by the NGV wakes. The existence of several harmonics indicates that the contribution of the stator wakes to Plane I is more complex than a simple sinusoidal function. On the other hand, the peak generated by the OGVs in fig. 4.4 (a) has almost no harmonics, which indicates the existence of a clear sinusoidal shape in the total pressure profile, as shown in fig. 4.3. Additionally, the strength of 30° and 6° harmonics can be

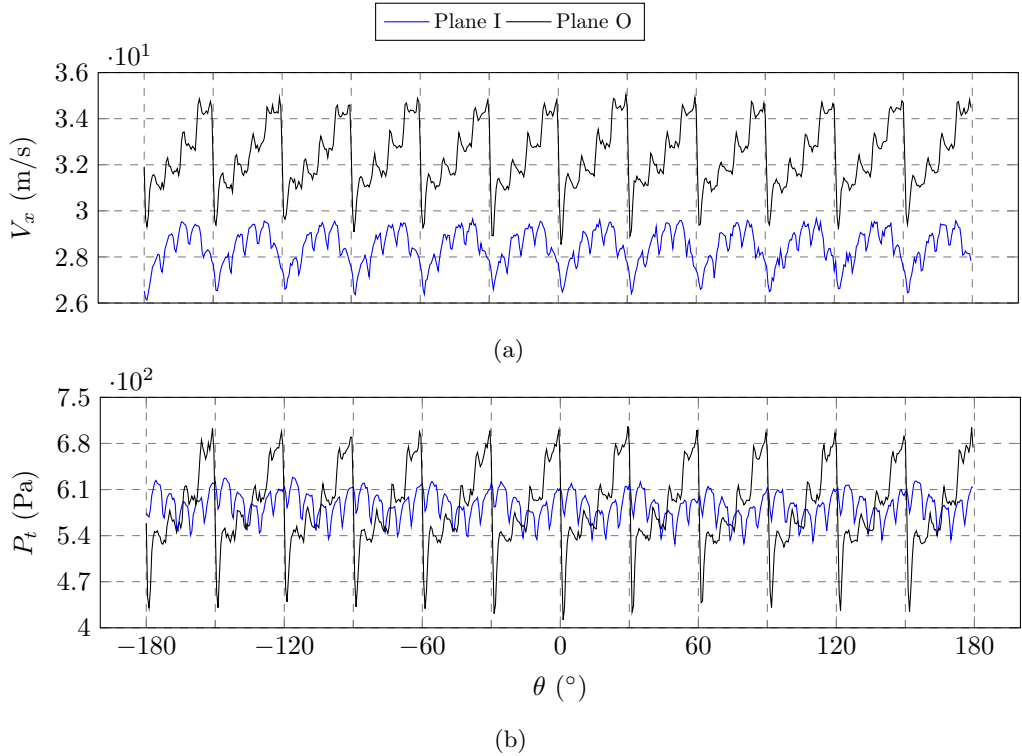


Figure 4.3: (a) Axial velocity mid-span profiles. (b) Total pressure mid-span profiles.

observed as well in the autocorrelation diagram shown in fig. 4.5 (a).

Furthermore, the axial velocity and total pressure profile at Plane O mid-span is more complex than at Plane I mid-span, but still 30° periodic looking at figs. 4.4 (b) and 4.5 (b). The existence of several harmonics from OGV and NGV wakes indicates that the total pressure distribution at Plane O mid-span is more complex than a combination of sinusoidal functions. However, since flow periodicity at Plane I and Plane O of the EES has been proved, 2-D sector analysis is performed to study the aerodynamics inside the EES and its performance.

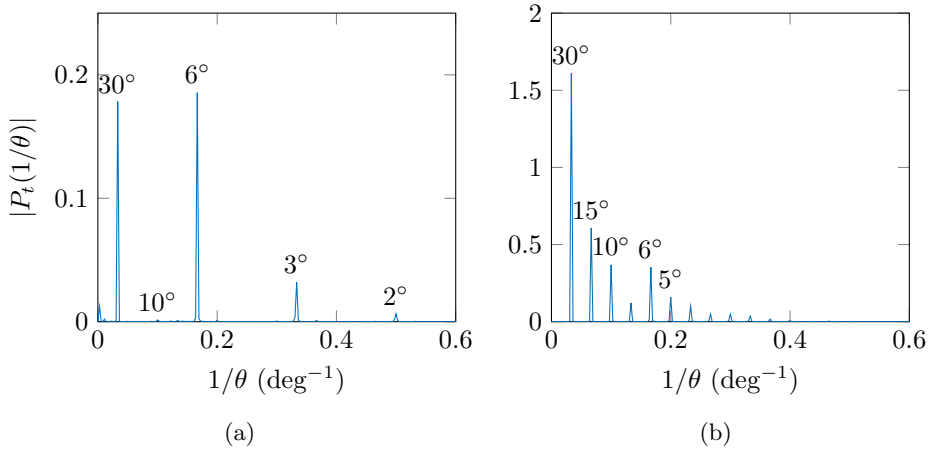


Figure 4.4: Power spectral density of total pressure at ADP 0 at midspan (a) Plane I and (b) Plane O.

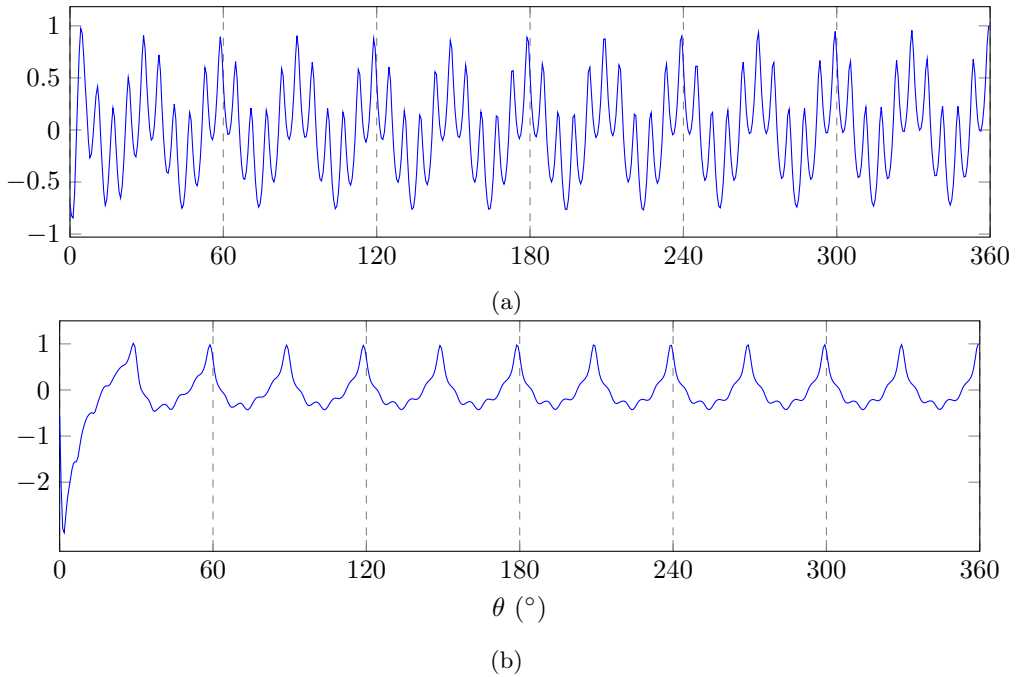


Figure 4.5: Normalized autocorrelation of total pressure at ADP 0 at midspan (a) Plane I and (b) Plane O.

4.3 Time-Averaged Flow field

Despite the unsteady structures created by the LPT rotor, time-averaged velocity components and pressure distributions provide a good insight into the main flow features. To analyze the flow, a five-hole probe at Plane I and a seven-hole probe at Plane O are used to perform the measurements. Furthermore, instrumented static pressure taps on the OGVs provide information regarding static pressure coefficients and, therefore, blade loading. Data from pressure taps will be shown in Section 4.5.

These experiments were performed at three different inlet conditions, summarized in table 4.1. During the experiments, flow coefficient (ϕ) and Reynolds number are kept constant regulating the centrifugal fan input power and oil system pressure. Note that ADP +10 and -10 represent cases of low and high EES loading respectively.

Table 4.1: Summary running conditions.

	ADP 0	ADP +10	ADP -10
V_x at stage inlet (m/s)	31.66	31.66	31.66
\dot{m} (kg/s)	23.55	23.55	23.55
T at stage inlet (K)	291.15	291.15	291.15
P_0 at stage inlet (Pa)	104133	104149	104005
Reynolds number channel height based (-)	465000	465000	465000
ψ (-)	1.153	0.933	1.462
ϕ rotor exit (-)	0.622	0.559	0.712
α at midspan rotor exit ($^\circ$)	-16.4	-6.4	-26.4
Rotational speed (rpm)	1088	951	1211
Power output (kW)	70.3	70.5	68.1

4.3.1 Inlet plane measurements

Figure 4.7 shows most representative variables measured at Plane I. First flow feature to be analyzed is the effect of the OGV leading edge over the Plane I, which is located about 35 mm upstream from the OGV leading edge. Looking at the static pressure coefficient, C_p , the position of the OGV's static pressure coefficient is shifted depending on the running conditions. This effect can be detected clearly in the swirl distribution as well. Moreover, due to the NGV wakes existing at this position, the interaction with the OGV leading edge is masked looking at other variables shown in fig. 4.7.

Another flow feature observed at Plane I is the tip leakage flow. Notwithstanding that most of the flow travels through the LPT rotor, a small fraction of it leaks through the

labyrinth sealing located on top of the shrouded blade. This tip leakage flow can easily be identified by looking at the swirl angle distribution from Plane I since the swirl angle is similar to the stator’s outlet swirl angle. Despite of tip leakage flow can be detected clearly, providing quantitative results with a multi-hole probe measurement technique are problematic because there are large gradients in this region and the location is close to the wall where pressure gradients can lead to a wrong value of, for example, yaw angle. Nevertheless, qualitative observations can be made such as the effect of the running conditions on size of the tip leakage flow region and NGV wakes interacting with it.

The wakes generated at the LPT stator can be observed from axial velocity and total pressure coefficient, even though they pass through a rotor stage. These wakes represent a major contribution to non-uniformity of circumferential profiles, as shown in fig. 4.4 (a).

Near the hub wall two pairs of rotating vortices are identified by looking at fig. 4.7 and shown in more detail in fig. 4.6. A similar pattern was also found at Chalmers’ low-speed, large-scale, high-pressure turbine facility, described in Arroyo [11]. Furthermore, near the shroud wall another vortex located at the tip of each NGV wake is found. The origin of this vortex is currently under discussion, although this vortex could be generated by the pressure gradient of the wake when it exits the shrouded blade. Other flow structures could be present in that region, but since the multi-hole probe measurement technique is limited in this area, other measurement techniques should be used to resolve all flow structures such as PIV measurements.

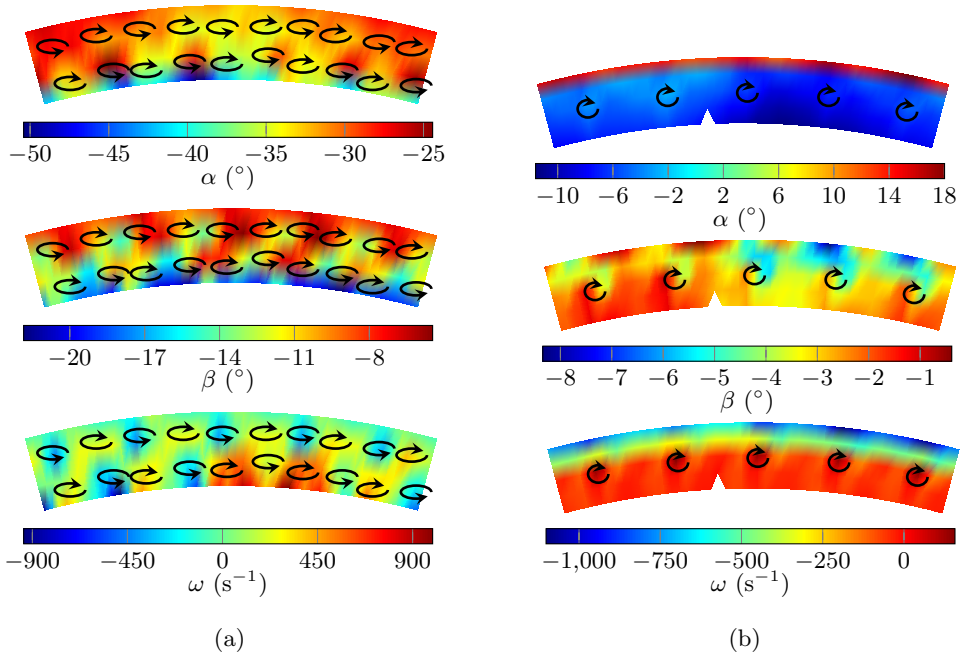


Figure 4.6: Zoom in from Plane I (a) hub region and (b) shroud region at ADP 0.

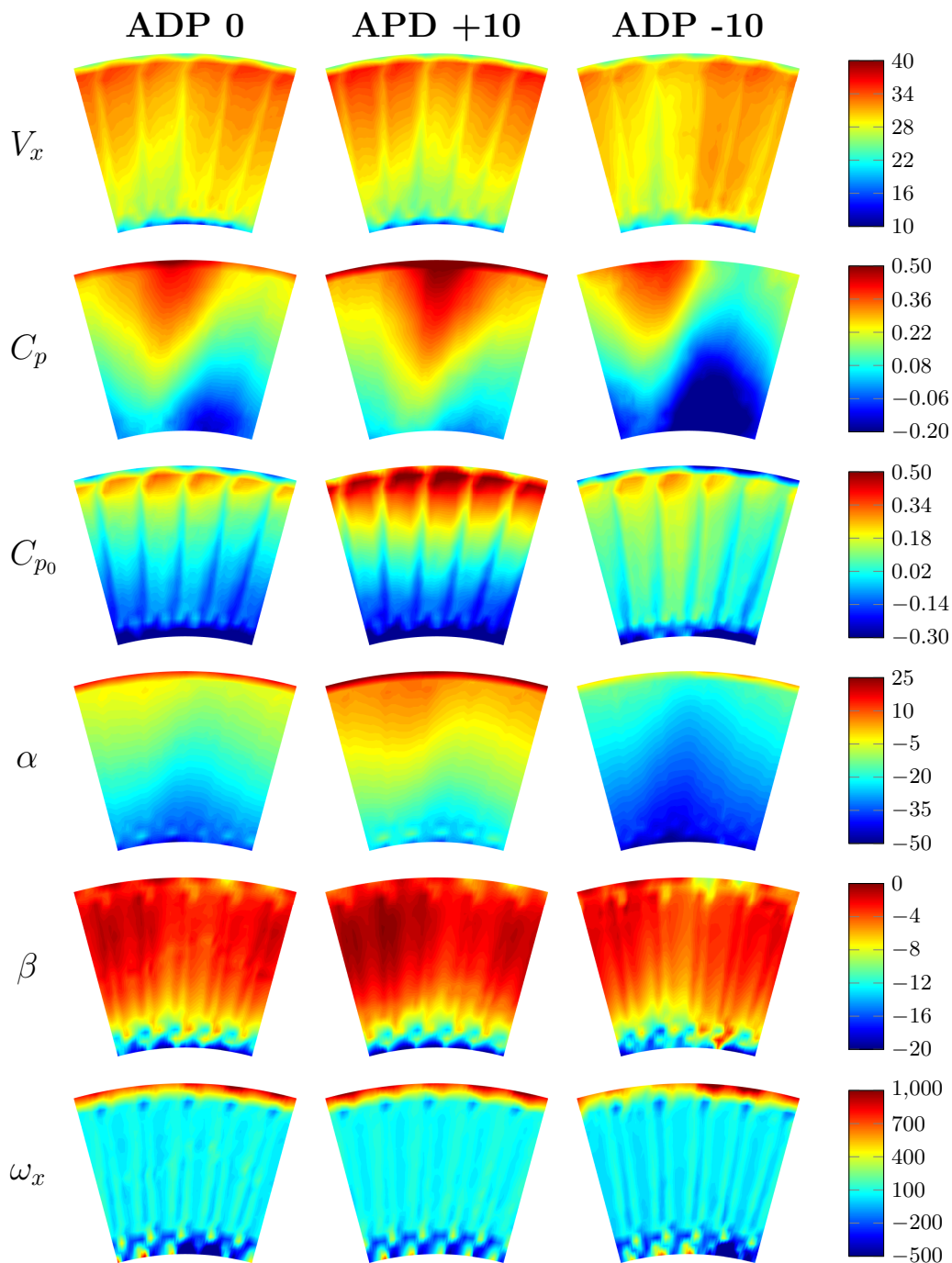


Figure 4.7: Flow data at Plane I. All variables are represented in SI units.

4.3.2 Outlet plane measurements

Figure 4.8 shows most representative variables measured at Plane O. At this location, the flow is intended to be fully axial. However, complex structures are developed due to boundary layer growth on the endwalls, NGV wakes traveling through the EES, boundary layer transition over the OGV, suction side flow reattachment, or flow separation which makes the flow in this region highly three dimensional.

Figure 4.9 shows the 2-D streamlines over the measurement plane. The main flow structure is the blade shed vortex at the trailing edge of the OGV. This vortex rotates counterclockwise and forces a counter rotating vortex through the main passage. The location of the vortex center changes with the inlet flow angle, moving towards the shroud when the inlet flow angle is more negative. Furthermore, hub vortices are clearly seen in fig. 4.9 (c). These two counter-rotating vortices have a clear impact over the location and size of the OGV vortex shed. Another structure located at the middle of the hub is a vortex that rotates clockwise. This vortex could be a horseshoe vortex generated at OGV LE, although additional measurements would be required to confirm this hypothesis. In addition, NGV wakes are still present at Plane O, although their strength has been decreased compared to the Plane I.

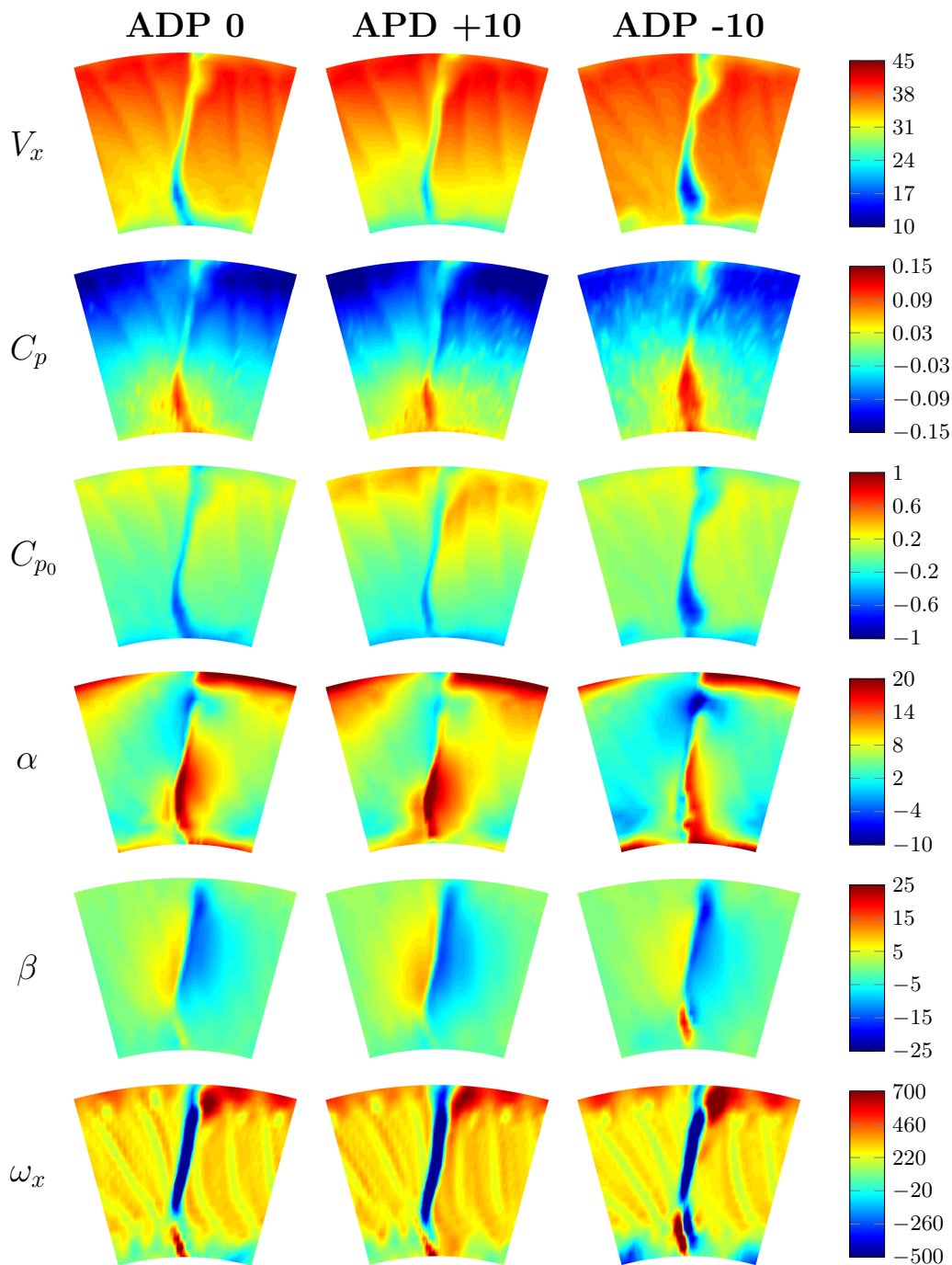
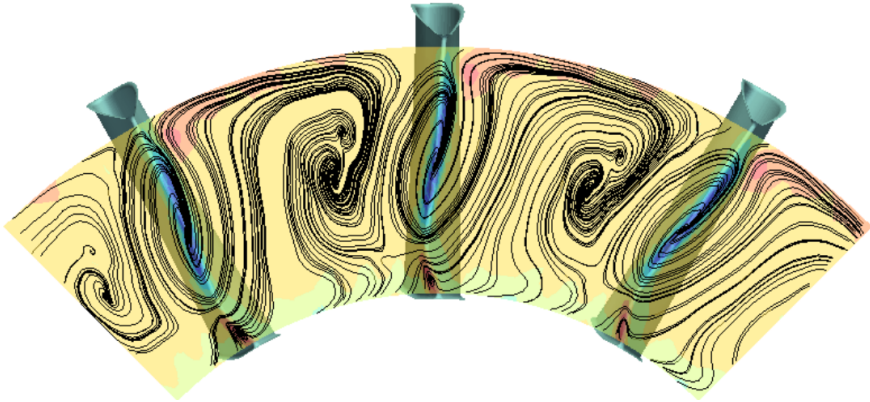
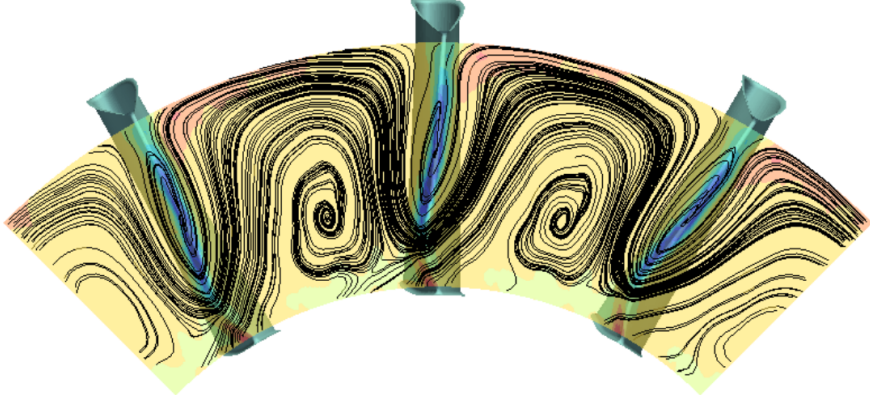


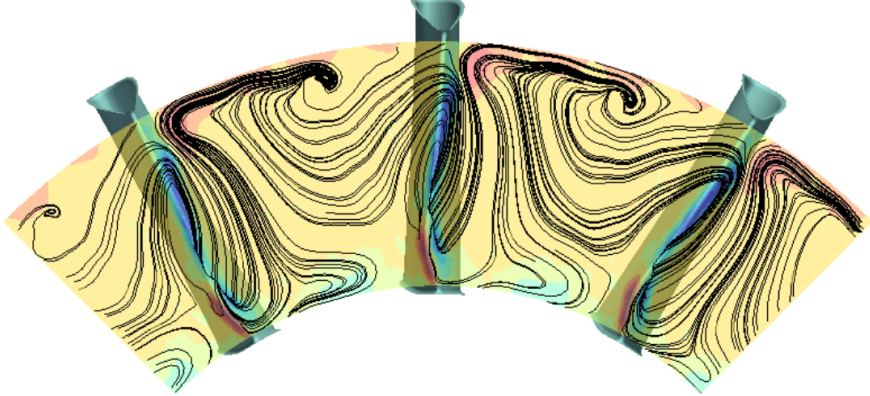
Figure 4.8: Flow data at Plane O



(a)



(b)



(c)

Figure 4.9: *Plane O vorticity and streamlines at (a) ADP 0, (b) ADP +10 and (c) ADP-10. Note that only one 30° sector was measured. All other sectors are instances of the same data set.*

4.4 Performance evaluation

One of the specifications for the rig design is the capability to measure pressure losses across one EES sector. There are several methods of evaluating aerodynamic performance or total pressure losses. The most common definition of pressure loss coefficient used in the field of fluid mechanics is shown in eq.4.7. Basically, pressure losses are scaled by the dynamic pressure at Plane I.

$$\zeta = \frac{\tilde{P}_{t,in} - \tilde{P}_{t,out}}{\tilde{q}_{in}} \quad (4.7)$$

However, Marn et. al. [27] suggests using the mass flow average pressure at Plane I, Plane O, and an exterior reference pressure for a rough estimation. This definition was used in a compressible LPT rig designed for similar purposes. Equation 4.8 represents the expression applied to this rig.

$$\zeta = \frac{\tilde{P}_{t,in} - \tilde{P}_{t,out}}{\tilde{P}_{t,in} - P_{ext}} \quad (4.8)$$

Since the definition of C_{p0} used at Chalmers' LPT-OGV rig facility corrects for pressure fluctuations during one run while adjusting the fan and braking power to fix the Reynolds number and flow coefficient, a pressure loss coefficient can be defined as a function of the total pressure coefficients. Equation 4.9 shows the expression of the pressure loss coefficient used at Chalmers' LPT-OGV rig.

$$\zeta = \tilde{C}_{p0,in} - \tilde{C}_{p0,out} \quad (4.9)$$

Note that to calculate the pressure losses from the pressure loss coefficient defined in eq. 4.9, eq. 4.10 is used.

$$\Delta P_t = \zeta \cdot q_{ref} \quad (4.10)$$

All definitions have been studied and compared for all operating conditions. Table 4.2 shows a summary of the performance evaluation study during NFFP6 AROS project campaign. The errors were estimated by applying the "Bulk" error values shown in table 3.4 and eq. 3.3 for calculating error on dependent variables. Several conclusions can be drawn from this study.

Table 4.2: Performance comparison at different operating conditions. Pressure losses are express in Pa.

	ADP 0		ADP -10		ADP +10	
	Experiment	CFD	Experiment	CFD	Experiment	CFD
ζ 4.7	0.0281	0.0295	0.0177	0.0334	0.0303	0.0317
ζ 4.8	0.0304	0.0284	0.0189	0.0412	0.0265	0.0313
ζ 4.9	0.0174	0.0238	0.0269	0.0332	0.0259	0.0274
$\varepsilon_{r,\zeta}$ 4.7, in %	29.4	-	44.0	-	30.8	-
$\varepsilon_{r,\zeta}$ 4.8, in %	28.9	-	44.5	-	30.3	-
$\varepsilon_{r,\zeta}$ 4.9, in %	50.5	-	32.7	-	34.0	-
$\tilde{P}_{t,in} - \tilde{P}_{t,out}$	18.45	18.28	12.48	27.00	17.45	20.60
$\Delta P_t = \zeta \cdot q_{ref}$	12.56	18.28	19.12	27.00	17.28	20.60

First, no matter which definition of error source is used, the relative error is approximately between 30% to 50%. Considering that the error from the pressure measurement unit is 2 Pa, near 10% of the maximum pressure losses measured, a large portion of the total error is already explained. Furthermore, comparing between all performance measurements and pressure losses, the only one that attributes largest pressure losses to the ADP-10 case was ζ from Chalmers' definition. To determine which case should generate the largest losses, OGV wake analysis is performed. Figure 4.10 shows the wake downstream of the OGV at different operating conditions and spans.

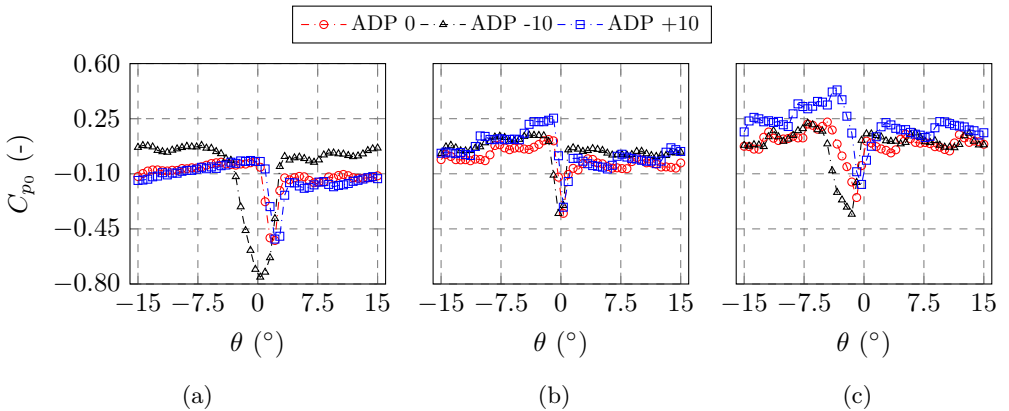


Figure 4.10: Total pressure coefficient downstream of the OGV at (a) 25%, (b) 50% and (c) 75% span.

Since the wake size at ADP-10 is substantially larger than the rest and assuming no large offsets on the total pressure coefficient at Plane I, the case that should produce the largest losses is ADP-10. In addition, results from CFD indicate the same trend, where the ADP-10 case has highest losses. In addition, CFD data also predicts higher losses at ADP+10 than ADP0. Due to these facts, ζ from eq. 4.9 is assumed to be more reliable than the other mentioned definitions in this facility.

4.5 CFD vs Experiments

The main purpose of this work is to provide experimental data to validate CFD tools. In this thesis, velocity and pressure distributions are compared with results from CFD simulations in order to estimate the fidelity of a commercial software to simulate the experiments performed. GKN Aerospace Sweden generated the airfoils' geometry using the in-house code VolVane, although the tip seal was added manually to the rotor blade, and the commercial software ICEM CFD as a structured mesh generator tool. The mesh size is 5.36 M cells is divided in three domains, stationary stator and EES and a rotating reference frame for rotor domain. Figure 4.11 shows the numerical grid used created at GKN Aerospace Sweden. The numerical mesh was created using the commercial software ICEM CFD.

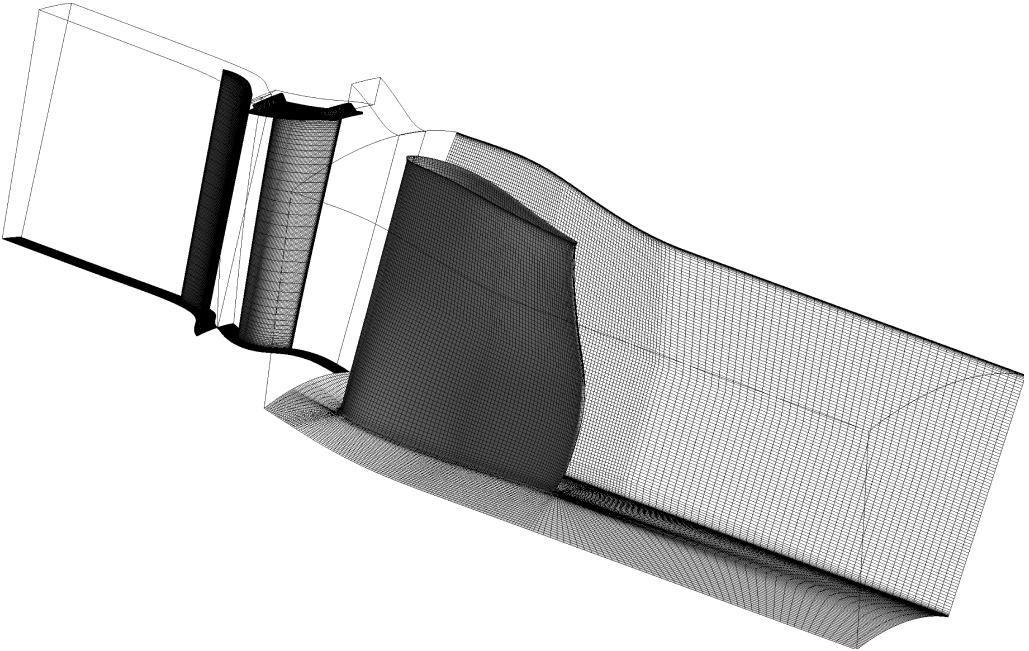


Figure 4.11: *Numerical grid of LPT 1.5 stage.*

Steady RANS simulations are performed at the same conditions as shown in table 4.1 using the commercial solver ANSYS CFX 16.2. Inlet mass flow and static pressure are

set at the inlet to the stator domain, rotational speed at rotor domain, and average static pressure at Plane O, the same as in the experiments. Turbulence model $k - \omega$ SST model is applied and y^+ is lower than one. Despite the LPT vane - LPT blade - OGV count for this EES configuration is 60-72-12 for full annulus or 5-6-1 for a 30° sector, only one NGV and rotor blade passage is discretized due to lower computational cost. Periodic boundary conditions in all domains are set and mixing plane at stator-rotor and rotor-EES interfaces. Note that Plane I intersects the rotor-EES interface, that is, the Plane I is inside the rotor and the EES domain. Hence, at Plane I, only circumferentially-averaged data will be compared while the Plane O radial and span profiles are analyzed.

Figure 4.12 shows radial distributions of C_{p0} , C_p and α at Plane I. ADP 0 and +10 running conditions are well predicted by the numerical simulation. However, at ADP-10 the total pressure coefficient distribution from CFD data is offset from experimental data. On the other hand, swirl angle distribution at Plane I is perfectly matched.

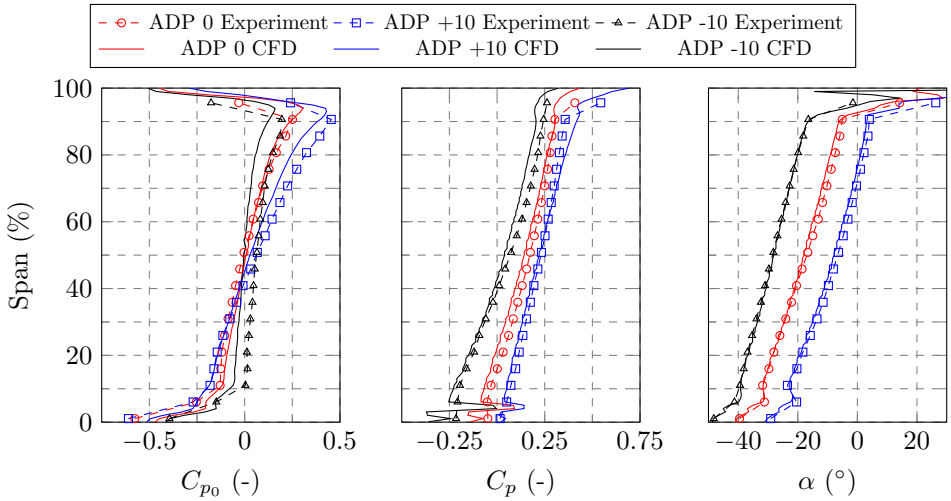


Figure 4.12: Circumferentially averaged profile from Plane I. Note that C_{p0} profile from CFD represents the average at rotor-OGV interface. Data near the hub wall falls inside the OGV stationary domain while the rest is inside the rotor domain.

Figure 4.13 shows radial distributions of C_{p0} , C_p and α at Plane O. Total pressure coefficient distributions are still matched by the numerical simulations for the ADP 0 and +10 running conditions. Moreover, at ADP -10, the same offset as in fig. 4.12 is present for the total pressure coefficient. However, static pressure distributions and swirl angle distributions are not matching the CFD predictions. Static pressure coefficients follow similar trends but offset. The same fact occurs for swirl angle distributions, since they are offset toward negative or close to zero average swirl angle at Plane O. Experimental results show a slight overturn of the flow compared to numerical data.

Despite showing good agreement between the experimental and numerical results over the circumferentially averaged profiles, fig. 4.14 shows large differences over span profiles. Note that positive and negative values of the azimuthal position represent the pressure

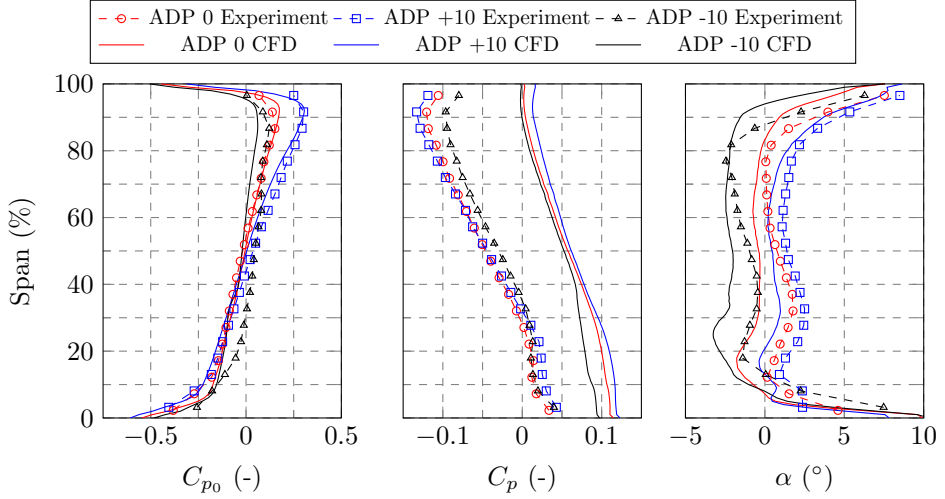


Figure 4.13: *Circumferentially averaged profile from Plane O.*

side and suction side of the OGV respectively. Qualitatively, the total pressure coefficient distributions are well predicted, although $k - \omega$ SST model overestimates wake thickness near the hub and the opposite near the shroud. Similar results are obtained from swirl angle distributions, except for the ADP -10 25% span case where swirl distribution is completely mismatched. It is interesting to highlight the good performance of the $k - \omega$ SST model at mid-span predicting distributions, wake thickness, and depth for all cases.

Also, fig. 4.15 shows the results from static pressure measurements and CFD simulations over the OGV surface. In general terms, there is good agreement between numerical and experimental data, especially at mid-span. Pressure peaks are well resolved in position and absolute value at the pressure side, while at the suction side only location is predicted with a high level of accuracy. Flow separation over the suction side of the OGV up to 50% span is predicted by CFD and experimental data at ADP -10. The turbulence model $k - \omega$ SST overestimates the size of the separation bubble. This fact explains the prediction of larger losses by the CFD simulation.

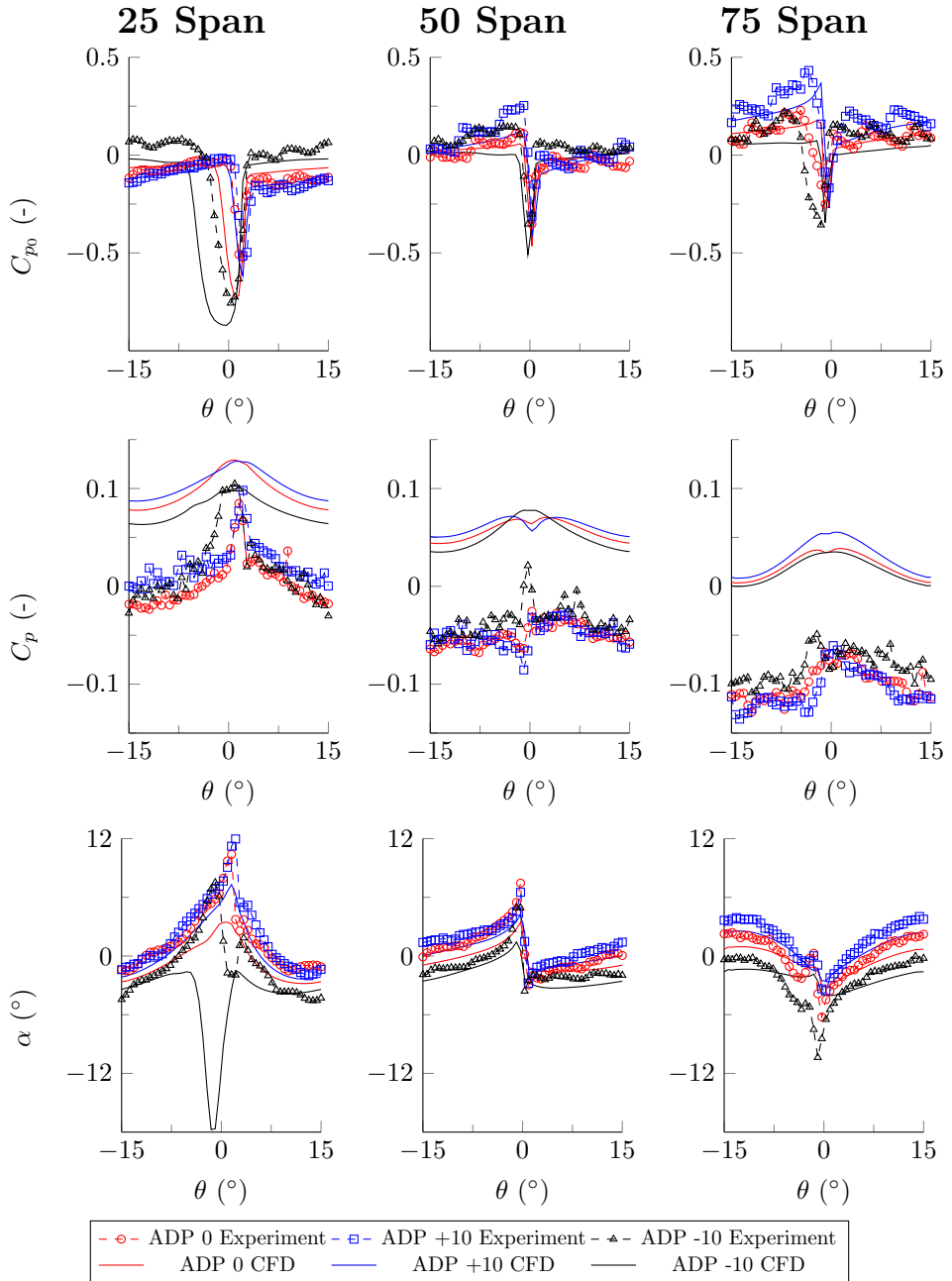


Figure 4.14: Total pressure coefficient, static pressure coefficient and swirl angle distributions at three different spans.

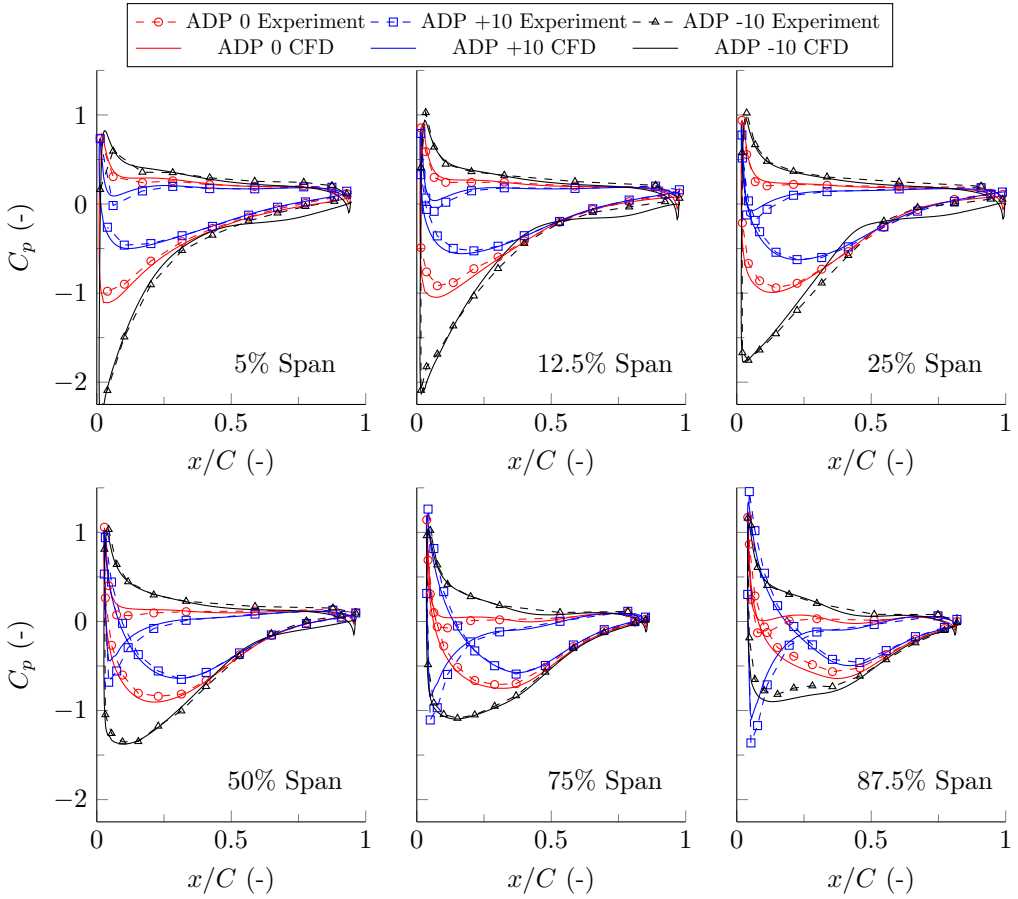


Figure 4.15: Pressure coefficient distribution along six different OGV spans.

5 Conclusions

This thesis presents a five years project at Chalmers University of Technology on the design, commissioning, and testing of a large-scale, low-speed LPT rig for investigating the flow inside an EES. The rig is designed using experimental correlations from classical low-speed wind-tunnel literature, experimental data from measurements taken in an existing rig, and numerical tools. The rig is designed in an iterative process considering physical and economic restrictions and optimizing structural and aerodynamic characteristics. These are cases in which none of the experimental correlations can provide a reliable approximate solution.

A new method for the design of an axisymmetric contraction duct with a central body is developed. Also, by means of CFD tools, the pressure-loss coefficient of the contraction section is evaluated for all operating points of the facility thereby adding precision to the measurement of mass flow.

FEA analysis is performed to study the most loaded components of the facility, and modal analysis is performed for the rotor turbine. Through these analyses, the safety of the rig and vibration-free operation is guaranteed. Moreover, deformations of the structural and aero components were calculated in order to guarantee that these deformations do not interact negatively with the flow quality, that is, affecting velocity or pressure distribution asymmetries in the LPT or test section.

Experimental data from the commissioning measurement campaign indicates a very low impact of the two rows of four structural struts each on the LPT inlet flow, and no evidence of the strut wakes was found at the test section inlet. In addition, flow periodicity is checked by means of mid-span velocity and pressure measurements and shown to successfully fulfill the quality requirements.

The thesis results provide a new experimental tool for evaluating novel EES designs under representative engine conditions and open up the potential of the new facility for future research of LPT-OGV flows for the aerospace industry

6 Contribution to Knowledge

This chapter presents a summary of all contributions to scientific community which the author considers new or worth for future discussion.

Despite of this thesis being focus on the design and testing of a state-of-the-art LPT-OGV facility, the author has dedicated some effort on developing heat transfer measurement techniques for future use in the new facility. Hence, contributions in both aerodynamics and heat transfer field have been made. These contributions to knowledge are listed below.

- Design of a state-of-the-art large-scale low-speed rig for turbomachinery research.
- Study of effect of turbulence screens on flow separation upstream their location.
- A new method on design of an axisymmetric contraction duct with a central body.
- Experimental aerodynamics data on a novel design of a EES is presented to scientific community for CFD validation purposes.
- Comparison between different definitions for pressure loss estimation from experimental data.
- Experimental heat transfer measurement techniques for steady flows.
- Transient temperature measurements of impinging jets at high temperature by means of an IR-camera.

7 Summary of Papers

This chapter provides a summary of all appended papers as well as the work done by the author in each paper. Moreover, an overall description of how each publication contributes to this thesis or future projects.

7.1 Overall Project Description

During the design (described in Paper A), manufacturing and assembly of the rig, efforts in developing IR and heat transfer measurement techniques for future use in the LPT-OGV rig have been done. Despite of not having time for implementing the acquired knowledge in the new experimental facility, four papers have been published from the work done.

In Paper B a heat transfer measurement technique applied to a highly 3-dimensional blade was tested. This heat transfer measurement technique has shown potential for being implemented at Chalmers' LPT-OGV facility for OGV heat transfer studies.

In Paper C a heat transfer measurement technique was applied to a flat 2-D OGV endwall inside Chalmers' large-scale low-speed OGV linear cascade facility. From this work a better understanding of OGV flows was obtained and a heat transfer measurement technique was tested. Some modifications would be performed before applying to this heat transfer measurement technique if it is implemented at Chalmers' LPT-OGV facility.

In Paper D and E PIV (performed by M. Bovo and M. Golubev) and transient temperature measurements were performed in an impinging jet over a flat aluminum cylinder. The main purpose of this work for future application at Chalmers' LPT-OGV facility is the development of an optical transient temperature measurements system and testing high temperature measurements. Calibration, non-uniformity correction and post-processing tools were developed for these purposes.

Furthermore, my work as supervisor of four MSc theses led to the publication of paper C and collaboration in experimental campaign for paper D and E.

In C. Jimenez (2013) [28] heat transfer and thermal measurement techniques were tested as well as the design of a flat endwall and optical access for heat transfer measurements.

In S. Llacer (2014) [29] an improved design of an endwall for heat transfer experiments was performed. In addition, aero measurements of OGV flows inside a linear cascade were performed.

In A. Barrachina (2014) [30] the application of IR temperature measurements through a silicon lens is investigated. Furthermore, experimental heat transfer measurements over an OGV were performed at Chalmers' low-speed large-scale OGV linear cascade facility. This work represents the first attempt to study heat transfer and transition phenomena over a state-of-the-art OGV at Chalmers' University of Technology.

In C. Urbiola (2015) [31] the assembly, validation and testing of an instrumented endwall for heat transfer measurements was performed.

7.2 Paper A

Facility for Investigating the Flow in a Low Pressure Turbine Exit Structure

Aim: To show the design of a state-of-the-art facility for investigating LPT-OGV flows.

Results: This publication shows the design process of Chalmers' LPT-OGV facility by means of CFD and empirical correlations. One of the most important results was the identification of risk of flow separation inside the diffusing section. The location and loss coefficient of a turbulence screen to avoid separated flow in the diffuser was determined in case flow uniformity measured at the outlet of the flow conditioning would indicate that such separation still affects flow uniformity negatively. In addition, a new method on the design of axisymmetric contractions with a central body was developed and explained in detail. This method was used in order to design the circular to annular contraction section. Finally, the conceptual design of the turbine and test section is shown in this paper.

Comments: Despite of presenting a preliminary version of the rig, this paper summarizes most of final component designs.

Division of Work: Borja Rojo did the conceptual design of this rig, CFD simulations for all components except LPT and FEA of blade, turbine section and wrote the paper. In addition, Borja Rojo developed the method on the design of axisymmetric contractions. Borja Rojo and Darri Kristmundsson did the CAD work. The other co-authors supervised and provided support regarding technical issues.

7.3 Paper B

Experimental Heat Transfer Study in an Intermediate Turbine Duct

Aim: To measure convective heat transfer coefficient over an intermediate turbine duct vane by means of IR-thermography.

Results: This publication shows the experimental work done in a large-scale low-speed high pressure turbine facility located at Chalmers University of Technology. Convective heat transfer coefficient measurement over an intermediate guide vane is successfully performed by measuring the intermediate guide vane surface temperature with an IR-camera which is isolated with a 5 mm silicone layer from an aluminum core at a uniform 60°C temperature distribution. The effect of neglecting radiative heat transfer coefficient is estimated to be around 5 to 10% at this operating condition, concluding the importance of analyzing this term even if the temperatures difference between the air flow and surface temperature is approximately 10 °C. Experimental results shows the large influence of tip flow leakage on the convective heat transfer coefficient distribution over the intermediate guide vane. In addition, experimental data was compared with CFD data concluding that both methods are far from matching specially at 90% span.

Comments: Originally, the intermediate guide vane was instrumented with an insulating epoxy layer. Due to the fact that this layer cracked twice after two different experiments, the authors concluded that gluing a silicone layer over the aluminum core would work. Since this layer was applied with five patches of silicone, some sharp discontinuities are observed in the results.

Division of Work: Borja Rojo calibrated the IR-camera, did the experimental set up together with Martin Johansson, carried out the experiments, post-process the data and wrote the paper. Martin Johansson performed the CFD simulations. The other co-authors supervised and provided support regarding technical issues.

7.4 Paper C

Experimental Heat Transfer Study of Endwall in a Linear Cascade with IR Thermography

Aim: To measure convective heat transfer coefficient over an endwall located inside a low-speed large-scale OGV linear cascade at different operating conditions.

Results: This publication shows the experimental work done in an large-scale low-speed OGV linear cascade located at Chalmers University of Technology. Convective heat transfer coefficient measurement over an OGV endwall is successfully performed by measuring the intermediate guide vane surface temperature with an IR-camera which is isolated with a 5 mm Plexiglass from an aluminum core at a uniform 60°C temperature distribution. The effect of Reynolds number at on-design case on the heat transfer coefficient has been studied concluding that at higher Reynolds number the convective heat transfer coefficient is increased. Furthermore, the convective heat transfer distribution does not change significantly. In addition, the effect of different inlet angles are studied on the convective heat transfer coefficient distribution. One conclusion of this study the stability of the convective heat transfer coefficient at 15° off-design angle. Finally, analyzing the convective heat transfer coefficient distribution at large off-design case, flow separation is observed.

Comments: At on-design and off-design 40° no horse shoe vortex could not be observed travelling through the blade passage. However, at off-design -25° there is a high heat transfer coefficient structure travelling from the pressure side to the suction side of the OGV. This structure could be horse shoe vortex, although aero measurements or oil flow visualization would confirm this hypothesis.

Division of Work: Borja Rojo and Carlos Jimenez calibrated the IR-camera, did the experimental set up and performed first tests of the endwall. Borja Rojo run the final experiments and wrote the paper. Valery Chernoray supervised and provided support regarding technical issues.

7.5 Paper D

Single Pulse Jet Impingement on Inclined Surface, Heat Transfer and Flow Field.

Aim: To study heat transfer and flow field from a single pulse impinging jet.

Results: First, understanding of the evolution of pulse impinging jet. Second, preliminary temperature distributions at different target angles by means of thermocouples located on the surface of the target and IR-thermography. Finally, preliminary CFD simulations were performed for comparing experimental and numerical data.

Comments: The main purpose of collaborating in this project is the development of transient temperature measurement tools by means of an IR-camera.

Division of Work: Mirko Bovo carried out PIV experiments and CFD simulations. Moreover, Mirko Bovo wrote the paper. Borja Rojo designed the experimental set up for transient temperature visualization for high temperatures and calibration tools. Special mention goes to Carlos Jimenez who run IR-thermography experiments as part of his MSc thesis, Maxim Golubev for execution of the PIV measurements and Eugenio De Benito Sienes.

7.6 Paper E

Measurements of a single pulse impinging jet. A CFD reference

Aim: To study heat transfer and flow field from a single pulse impinging jet.

Results: A comprehensive experimental study of velocity field and turbulence intensity for impinging jets is performed. Furthermore, a detailed experimental study of temperature distributions over the target surface. Temperature distributions obtained from thermocouples located on the surface of the target and IR-thermography are compared. Moreover, the influence of the relative angle between the target and the impinging jet is characterized.

Comments: Results from this experimental study were used afterwards for CFD validation by M. Bovo and L. Davidson [32].

Division of Work: Mirko Bovo carried out PIV experiments and CFD simulations. Moreover, Mirko Bovo wrote the paper. Borja Rojo designed the experimental set up for transient temperature visualization for high temperatures and calibration tools. Special mention goes to Carlos Jimenez who run IR-thermography experiments as part of his MSc thesis, Maxim Golubev for execution of the PIV measurements and Eugenio De Benito Sienes.

Bibliography

- [1] <http://www.pw.utc.com>. Accessed: 2017-08-06.
- [2] R. Goldstein and R. Spores, “Turbulent transport on the endwall in the region between adjacent turbine blades,” *Journal of Heat Transfer*, vol. 110, no. 4a, pp. 862–869, 1988.
- [3] T. Selic, D. Lengani, A. Marn, and F. Heitmeir, “Aerodynamic effects of an unshrouded low pressure turbine on a low aspect ratio exit guide vane,” *Journal of Turbomachinery*, vol. 8, no. 12, pp. 1275–1286, 2012.
- [4] A. Marn, T. Selic, F. Schönleitner, F. Heitmeir, and D. Broszat, “Comparison of the aerodynamics of acoustically designed EGVs and a state-of-the-art EGV,” no. 45608, p. V02AT41A005, 2014.
- [5] J. Seda, “Aircraft engine with inter-turbine engine frame,” Mar. 23 2004. US Patent 6,708,482.
- [6] T. Sonoda and H.-A. Schreiber, “Aerodynamic characteristics of supercritical outlet guide vanes at low reynolds number conditions,” *Journal of Turbomachinery*, vol. 129, no. 4, pp. 694–704, 2007.
- [7] J. Hjärne, J. Larsson, and L. Löfdahl, “Design of a modern test-facility for LPT/OGV flows,” in *ASME Turbo Expo 2003, collocated with the 2003 International Joint Power Generation Conference*, pp. 137–145, American Society of Mechanical Engineers, 2003.
- [8] J. Hjärne, *Turbine Outlet Guide Vane Flows*. PhD thesis, Chalmers University of Technology, 2007.
- [9] B. Rojo, C. Jimenez, and V. Chernoray, “Experimental heat transfer study of endwall in a linear cascade with IR thermography,” in *EPJ Web of Conferences*, vol. 67, p. 02100, EDP Sciences, 2014.
- [10] F. Schönleitner, H. Koch, T. Selic, M. Hoeger, and A. Marn, “Comparison of the experimental results between a 2D EGV cascade test and a rig test under engine representative conditions,” in *ASME Turbo Expo 2014: Turbine Technical Conference and Exposition*, pp. V02CT38A053–V02CT38A053, American Society of Mechanical Engineers, 2014.
- [11] C. Arroyo, *Aerothermal investigation of an intermediate turbine duct*. PhD thesis, Chalmers University of Technology, 2009.
- [12] P. Bradshaw and R. Pankhurst, “The design of low-speed wind tunnels,” *Progress in Aerospace Sciences*, vol. 5, pp. 1 – 69, 1964.
- [13] J. Barlow, W. Rae, and A. Pope, *Low-Speed Wind Tunnel Testing*. Aerospace engineering, mechanical engineering, Wiley, 1999.

- [14] R. D. Mehta and P. Bradshaw, "Design rules for small low speed wind tunnels," *The Aeronautical Journal*, vol. 83, no. 827, pp. 443–453, 1979.
- [15] T. Morel, "Comprehensive design of axisymmetric wind tunnel contractions," *Journal of Fluids Engineering*, vol. 97, no. 2, pp. 225–233, 1975.
- [16] M. Mikhail, "Optimum design of wind tunnel contractions," *AIAA journal*, vol. 17, no. 5, pp. 471–477, 1979.
- [17] M. Abbaspour and M. Shojaee, "Innovative approach to design a new national low speed wind tunnel," *International Journal of Environmental Science & Technology*, vol. 6, no. 1, pp. 23–34, 2009.
- [18] R. D. Mehta and J. H. Bell, "Boundary-layer predictions for small low-speed contractions," *AIAA journal*, vol. 27, no. 3, pp. 372–374, 1989.
- [19] G. Chmielewski, "Boundary-layer considerations in the design of aerodynamic contractions," *Journal of Aircraft*, vol. 11, no. 8, pp. 435–438, 1974.
- [20] <http://http://www.parker.com>. Accessed: 2017-06-30.
- [21] <http://www.brookcrompton.com>. Accessed: 2015-10-13.
- [22] B. Rojo, V. Chernoray, M. Johansson, and M. Golubev, "Experimental heat transfer study in an intermediate turbine duct," in *49th AIAA/ASME/SAE/ASEE Joint Propulsion Conference*, 2013.
- [23] C. Arroyo, L.-U. Axelsson, U. Håll, T. G. Johansson, J. Larsson, and F. Haselbach, "Large scale low speed facility for investigating intermediate turbine duct flows," in *44th AIAA Aerospace Sciences Meeting and Exhibit, AIAA-2006-1312*, 2006.
- [24] L.-U. Axelsson, *Experimental investigation of the flow field in an aggressive intermediate turbine duct*. PhD thesis, Chalmers University of Technology, 2009.
- [25] C. Tropea and A. L. Yarin, *Springer handbook of experimental fluid mechanics*, vol. 1. Springer Science & Business Media, 2007.
- [26] L. E. Steen, J. F. VanZante, A. P. Broeren, and M. J. Kubiak, "Flow quality surveys in the settling chamber of the NASA Glenn Icing Research Tunnel (2011 tests)," 2012.
- [27] A. Marn, D. Broszat, T. Selic, F. Schönleitner, and F. Heitmeir, "Comparison of the aerodynamics of acoustically designed exit guide vanes and a state-of-the-art exit guide vane," *Journal of Turbomachinery*, vol. 137, no. 4, p. 041002, 2015.
- [28] C. Jimenez, "Experimental heat transfer studies with infrared camera," MSc Thesis, Chalmers University of Technology, 2013.
- [29] S. Llacer, "Design of instrumented end-wall for heat transfer measurements in a low-speed linear cascade and flow measurements," MSc Thesis, Chalmers University of Technology, 2014.

- [30] A. Barrachina, “Heat transfer studies with IR thermography techniques,” MSc Thesis, Chalmers University of Technology, 2014.
- [31] C. Urbiola, “Experimental heat transfer measurement technique validation and measurements in a linear cascade of an OGV and endwall,” MSc Thesis, Chalmers University of Technology, 2015.
- [32] M. Bovo and L. Davidson, “Direct comparison of LES and experiment of a single-pulse impinging jet,” *International Journal of Heat and Mass Transfer*, vol. 88, pp. 102–110, 2015.

Appendices

A Pictures from Chalmers LPT-OGV rig



Figure A.1: *Metallic screen mounting. "High tec" pretension system.*



Figure A.2: *Experimentalist excited setting up first aero measurement for commissioning.*



Figure A.3: *Fresh LPT rotor.*



Figure A.4: *Clocking the LPT rotor shroud.*

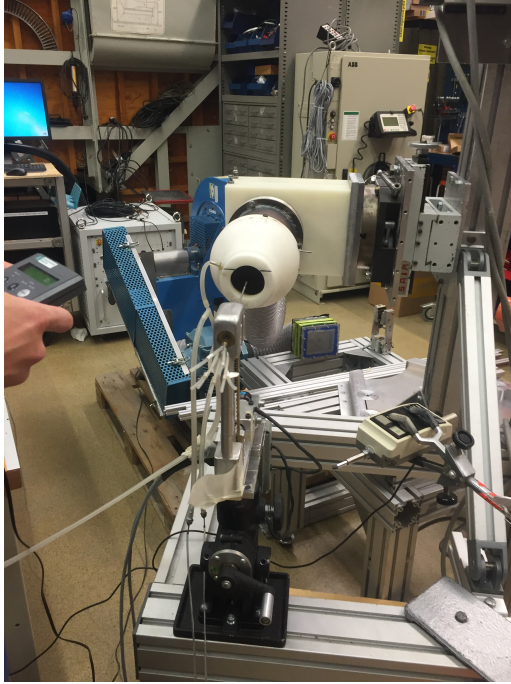


Figure A.5: *7-hole probe calibration set up.*



Figure A.6: *Calibrating traversing system over reference points.*



Figure A.7: Facility assembled. Isak Jonsson is inspecting the traversing system. He is near 2m tall (this information is only provided for scaling purposes of the picture).



Figure A.8: *EES after last experiment. The end.*

